3-3 X-ray Correlation Photoacoustics for Depth Resolved Analysis of Layered Materials

Introduction

Correlation photoacoustic spectra of the first kind[24,33] provides information on the thermal and structural properties of the sample, since the signal from the surface layer has a short delay time while that from the deep layer has a longer delay time. Although the conventional photoacoustic method gives similar information by the use of the phase delay technique[6,7], the cross correlation method gives more detailed and straightfoward information than the conventional one for understanding the thermal and structural properties of multi layered samples. Moreover, within the conventional technique which uses a regular interval modulation system, if the output signal contains a number of components with different delay times, one cannot virtually separate each component since they are observed as a composite signal both in phase and amplitude.

It is noted, in the present study, that both an X-ray tube and synchrotron radiation are used as excitation sources. X-ray photoacoustic measurements using a conventional X-ray tube as an excitation source can be easily conducted, and is very convenient when combined with other techniques such as X-ray fluorescence etc.[9,37,38].

Apparatus

Figure 3-3-1 is a schematic diagram of the experimental arrangement. The photoacoustic cell used has beryllium windows and is similar to that described in a previous chapter(3-2). A monochromatic X-ray beam, white X-ray beam and visible light beam were used as excitation sources. The experiment involving the use of a excitation of monochromatic X-ray beam was conducted at beam line BL-10C at the Photon Factory (National Laboratory for High Energy Physics, KEK, Tsukuba), and was monochromated to 1.30Å or 1.48Å and focused to a 3mm×2mm area on the samples. The white X-ray beam was from a built-in type X-ray tube with a copper target (40KV, 20mA) and was narrowed and collimated by a lead collimator with a diameter of about 8mm. In the case of the photoacoustic measurements with visible light excitation, the upper beryllium window of the cell was replaced with a quartz window of 1mm thickness. The light beam from a 500W xenon arc lamp was filtered with the use of UV cut (TOSHIBA, Y44) and IR cut (TOSHIBA, IRA-25S) filters and was focused to spots of 2 to 13mm diameter on the specimen. A mechanical random chopper containing two M-series of pseudo random binary sequence (n=31, where n is a number of on-off units in one series) was used to modulate the excitation beam. Chopper speed was varied from 1.2 to 4 rotation per second (RPS). In this experiment, the time

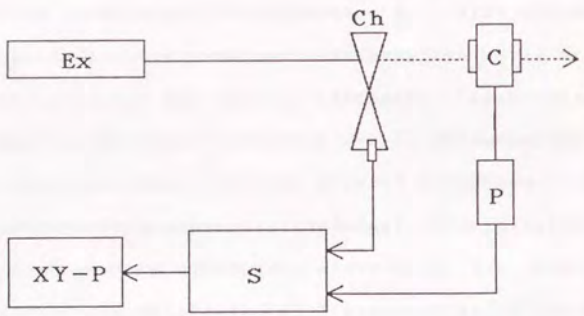

Fig. 3-3-1. Schematic diagram of the experimental arrangement. Ex, excitation beam (monochromated X-ray beam of synchrotron radiation, white X-rays from X-ray tube with copper target or visible light from Xe arc lamp); Ch, M-series random chopper; C, photoacoustic cell; P, preamplifier; S, FFT signal analyzer; XY-P, XY-plotter.

resolution of the measuring system was determined by the rotating speed of the chopper and number of on-off units in the chopper blade, and was calculated to be 13 or 4ms ($1/2nr$), n=31, r=1.2 or 4, where r is the rotational speed of the chopper. The reference signal was obtained at a photocoupler installed at the chopper. The preamplified photoacoustic signal and the reference signal from the chopper were introduced into a FFT analyzer (ADVANTEST, TR9403), where the calculation of cross correlation between these signals was conducted and integrated up to 128 times.

Sample materials

Figure 3-3-2(a-c) shows the model samples, types I, II, and III, used in the present study. The type I sample consists of laminated layers of lead (thickness 100μm, diameter 18mm) and aluminum(thickness about 15μm, diameter 18mm) foils. The aluminum foil was adhered on both sides of the lead foil by polymer resin. The prepared samples are referred to as I-0, I-1, I-2 and I-3 depending on the number of aluminum layers, n, on each side of the lead foil. The type II samples were the laminated samples of lead (thickness 100μm, diameter 18mm) and polymer adhesive films (poly-propylene base, thickness about 50μm, diameter 18mm). The polymer adhesive films were adhered on both sides of the lead foil. These samples are referred to as II-0, II-1, ...

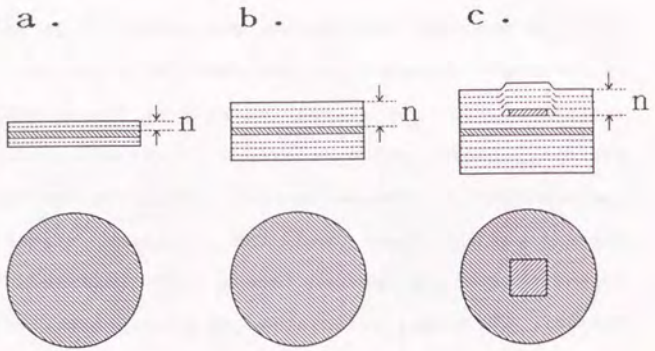

Fig. 3-3-2. Cross section and top view of the samples. Samples of type I (a) are laminated samples of lead and aluminum foils. The number of aluminum layers was 0 to 3 on each side of the lead foil. Sample I-2 is shown in this figure as an example. Samples of type II (b) are laminated samples of lead and polymer adhesive films. The number of polymer layers was 0 to 6 on each side of the lead foil. Sample II-4 is shown as an example. Samples of type III (c) are laminated samples of lead and polymer adhesive films with small intermediate lead foil layer near the surface of the polymer layer and a larger and deeper lead layer between the polymer layers. Sample III-4 is shown as an example.

and II-6 depending on the number, *n*, of the polymer layers on each side of the lead foil. The type III samples are similar to sample II-6, but they have a surface or intermediate lead foil layer (thickness about 100μm, size about 3×3mm) on the surface of the polymer layer or between the polymer layers. Thus sample III-6 is equivalent to sample II-6. They are referred to as III-0, III-1, ... and III-6 depending on the number of polymer layers, *n*, on the intermediate lead layer.

Results and discussion

Figure 3-3-3 shows the correlation photoacoustic spectra of the laminated samples of aluminum and lead foil (type I samples) measured with a monochromated X-ray beam of 1.30 and 1.45Å at a chopping speed of 4RPS. The time τ_o is defined as the time interval between the excitation and the top peak. Two peaks were observed at τ_o values of 10ms and 70ms in the spectra for sample I-3. For sample I-2, a shoulder peak was observed at a τ_o value of approximately 50ms. The first peak is considered to be due to heat generated in the surface aluminum layer. The second peak and the shoulder peak are considered as originating from the lead layers. Figure 3-3-4 show plots of τ_o *versus* the number of aluminum layers. The τ_o value for the first peak does not show any change with the increase of aluminum

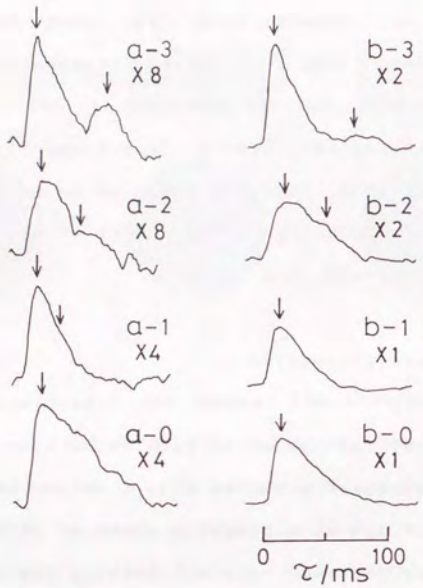

Fig. 3-3-3. Correlation photoacoustic spectra (impulse response curves) of type I samples.
a, spectra obtained by 1.30Å excitations, and b, spectra obtained by 1.45Å excitation. Symbols a-0 to a-3 (or b-0 to b-3) correspond to the spectra of samples I-0 to I-3. Peak positions are indicated by arrows.

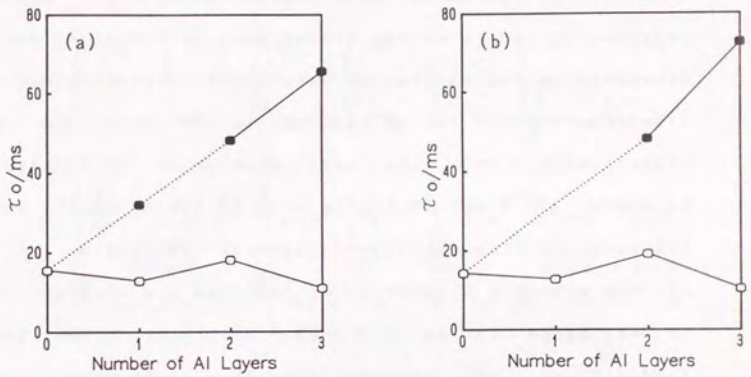

Fig. 3-3-4. Dependence of τ_o of sample type I on the number of the aluminum layers measured at 1.30Å (a) and 1.45Å (b).
—○—○— : τ_o for the first peak;
—●—●— : τ_o for the second peaks.

layers, while the second peak and the shoulder peak increase with the number of aluminum layers. The dependence of τ_o on the number of aluminum layers did not change as a function of excitation wavelength. On the other hand, the relative intensity of the second peak to the first peak was dependent on the excitation wavelength. Transmittance of the aluminum layer is calculated to be 69.8 and 61.0%, respectively, from the mass absorption coefficient of aluminum (29.6 and 40.7cm²/g at 1.30 and 1.45Å)[1] and the thickness of aluminum layer (15μm×3). Therefore, the ratio of the absorbed X-ray flux in the lead and aluminum layers is estimated to be 2.3 (=69.8/30.2) at 1.30Å and 1.6 (=39/61) at 1.45Å, respectively. This is in good agreement with the observed results in that the intensity of the second peak in the correlation spectra at 1.30Å is large compared to that at 1.45Å. In the experiment with excitation by white X-rays, the second peak was not observed probably due to the fact that the peak is immersed in noise because absorption occurring in surface aluminum layer is large (50.2cm^2/g) for characteristic copper X-rays (Cu K_α 1.54Å). These experimental results suggest that the signal from deep layers also gives information about the optical properties of the surface layer.

Figure 3-3-5 shows a correlation photoacoustic spectra of the laminated samples of polymer adhesive film and lead

Fig. 3-3-5. Correlation photoacoustic spectra of type II samples (a) and type III samples (b) measured with white X-ray excitation. Symbols a-0 to a-6 (or b-0 to b-6) correspond to the spectra of samples II-0 to II-6 (or III-0 to III-6) respectively. Peak positions are indicated by arrows. Magnification of the spectra is ×1 for a-0, a-1 and b-0, ×2 for b-1, ×4 for a-2, a-3, a-4, b-2 and b-5, ×8 for the others.

foil (type II (a) and type III (b) samples) measured with excitation by white X-ray at a chopping speed of 1.2RPS. Two types of peaks, the first sharp peak and the second broad peak were also observed for the type I samples. However, in the sample III-2 spectra a third peak was also found, though somewhat obscured it because of a low signal to noise ratio. The third peak is considered to be assigned to the heat from the intermediate lead layer. Figure 3-3-6 show plots of τ_o *versus* the number of polymer layers. The τ_o value for the first peak show no change with an increase in the number of polymer layers. However, the second peak and the shoulder peak increased with the number of polymer layers. Correlation spectra of the samples with a large number of polymer layers is noisy so that the observed τ_o value is ambiguous to some extent. However, there is a slight difference in the signal dependencies on the number of polymer layers between type II and type III samples. The change for the type II samples shows a monotonous increase, while that for type III samples shows a plateau in the large n region.

Figure 3-3-7 shows the correlation photoacoustic spectra measured for the laminated samples of polymer adhesive films and lead foils (type III samples) by visible light excitation with various diameters at a chopping speed of 1.2RPS. Two types of peaks, a sharp peak and a broad one

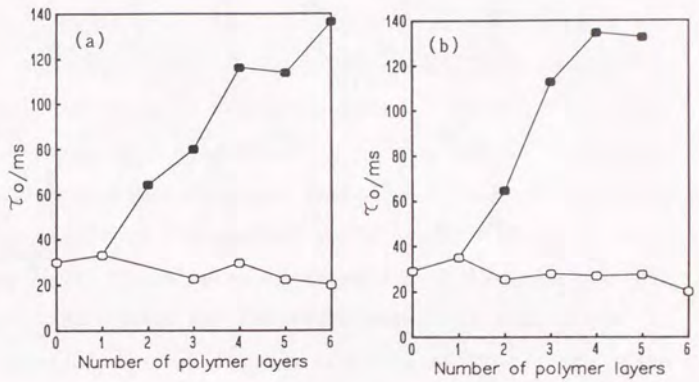

Fig. 3-3-6. Dependence of τ_o of type II samples (a) and type III samples (b) on the number of polymer layers measured with white X-ray excitation.

—○—○— : τ_o for the first peak;

—●—●— : τ_o for the second peak.

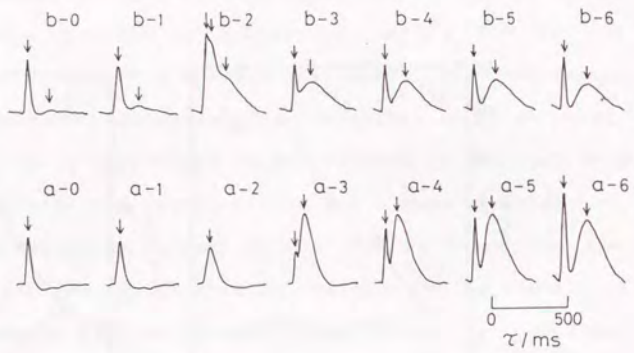

Fig. 3-3-7. Correlation photoacoustic spectra of type III samples measured with visible light beam of 2mm (a) and 13mm (b) diameter. The symbols a-0 to a-6 (or b-0 to b-6) correspond to spectra for samples III-0 to III-6 respectively. Peak positions are pointed with arrows. Magnification of the spectra is ×2 for a-3, a-4, a-5, a-6 and b-2, and ×1 for the others.

were observed in the measurement with excitation at a beam diameter of 2mm. This is similar to the case of type II samples excited by X-rays. The 2mm diameter beam was focused on the intermediate lead layer, so that the photoacoustic signal originated only from the surface and the intermediate layers. Therefore, the correlation spectra are considered to be equal to those of type II samples. On the contrary, with excitation at a beam diameter of 13mm which irradiates both the intermediate and deep lead layers, a third shoulder peak was found in the spectra for sample III-2 as in the case of type III samples observed by X-ray excitation. The first, the second and the third peaks are considered as being assigned to the surface layer on the top, the lead layer at a deep level and the intermediate lead layer, respectively. Figure 3-3-8(a) show plots of τ_o values *versus* the number of polymer layers for measurements with an excitation beam diameter of 2mm. τ_o values for the first sharp peaks remains constant, while those for the second peaks increase monotonously with the number of polymer layers. Figure 3-3-8(b) show plots of τ_o on the number of polymer layers for measurements with excitation at a beam diameter of 13mm. τ_o values for the first and the second peaks do not show any change with an increase in the number of polymer layers except for the second peak for sample II-3 (n=3). The observed τ_o for the third shoulder peak

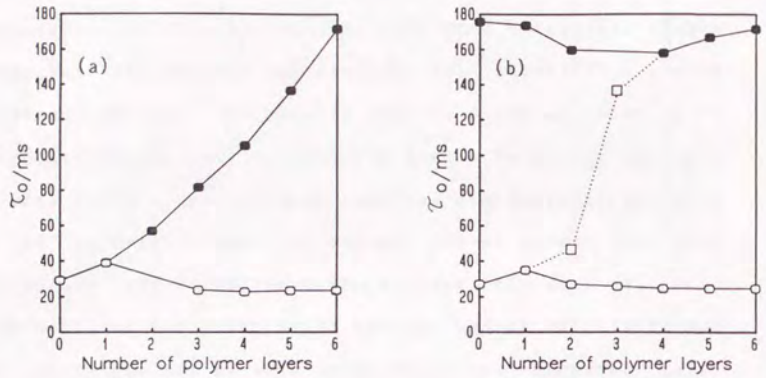

Fig. 3-3-8. Dependence of τ_o for type III samples on the number of polymer layers measured with a visible light beam of 2mm (a) and 13mm (b) diameter.

—○—○— : τ_o for the first peaks;

—●—●— : τ_o for the second peak;

···□···□··· : τ_o for the third peak.

corresponds to the level between the surface layer and the deep layer. Since τ_o value of the second peak for sample II-3 is slightly smaller than that for the other samples, this peak seems more likely to correspond to the third peak for sample II-2. Thus the change of τ_o value for the peak corresponding to the intermediate layer is given as a dotted line. τ_o increases with the number of polymer layers and shows a plateau in the large n region. The change is similar to the case where measurements are made with a collimated white X-ray beam of 8mm diameter. This confirms that the shoulder peak in the X-ray measurement is due to heat from the intermediate lead layer.

Based on the experimental results given so far, the signal delay time τ_o is related to the depth at which heat is generated in the sample, and that thermal characteristics of sample are reflected in the relation between τ_o and the sampling depth. However, the peak becomes broader and weaker with an increase in the depth of heat generation because the heat diffuses through the material. Therefore, observation of this peak depends on the signal intensity and the depth of heat generation. Further, resolution of two or more peaks depends on the relative intensity and the relative depth of heat generation. In the case where the third peak is observed from the intermediate lead layer, signals with a τ_o value of approximately three times as large as the first

peak. The τ_o for the third peak is also approximated 1/3 times the value of the τ_o for the second peak.

3-4 X-ray Correlation Photoacoustic Spectra near the Absorption Edge

Introduction

The X-ray absorption coefficient for a given material changes greatly at the absorption edge, thereby also changing the depth of heat generation. Therefore, measurements of the correlation photoacoustic spectra near the X-ray absorption edge clarifies the characteristics of bulk samples. It is also of interest whether correlation spectra show fine structure near the absorption edge.

Experimental

The experiments were made with synchrotron radiation at beam line (BL-10C) at KEK. The X-ray beam was modulated by a mechanical random chopper (containing 2 series of M-sequence, n=31). The experimental arrangement and photoacoustic cell used was similar to that used in previous sections. The photoacoustic cell was placed on a pneumatic floating table. The preamplified photoacoustic signal and reference signal from the chopper were introduced into an FFT analyzer (ADVANTEST, TR9403), where the cross correlation between these signals was calculated. The correlation spectra was integrated up to 1024 times. In this experiment, the time resolution of the measuring system is

fixed by the rotational speed of the chopper, r, and the number n of on-off units in the chopper blade, and is calculated to be 4ms ($1/2nr$, n=31, r=4).

Results and Discussion

Correlation photoacoustic spectra for copper foils (thickness 10, 50, 200 and 1000μm) were measured at wavelengths between 1.32 and 1.45Å. Although the penetration depth of the X-ray beam in the copper foil changes from 4 to 28μm when the wavelength is changed from 1.35 to 1.40Å across the absorption edge[1], τ_o showed no significant change as seen in Fig. 3-4-1. This seems to be due to the lack of time resolution in the measuring system. Figures 3-4-2 and 3-4-3 show the changes of τ_f and I_{max} as a function of X-ray wavelength. I_{max} shows a sharp drop at the absorption edge for each thickness, and τ_f shows a rise at the absorption edge for the samples with thicknesses of 50 and 200μm. These results show that 1) τ_o is not dependent on the absorption coefficient of the sample but on the sample thickness; 2) τ_f and I_{max} are dependent on both the absorption coefficient and thickness of the sample. Traces of I_{max} for foils of 50, 200, 1000μm thickness show periodic change in the region from 1.32Å to 1.38Å. The period is about 0.03Å in this experiment and is reduced to about 200eV in electron energy. This value is large compared

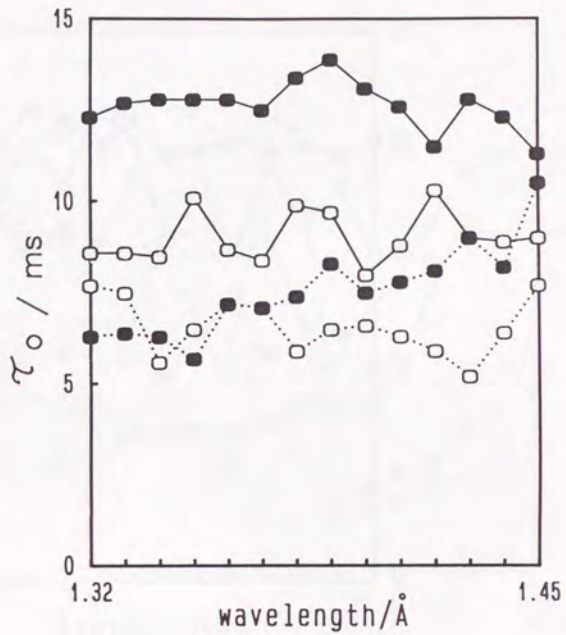

Fig. 3-4-1 Dependence of τ_o on X-ray wavelength for copper foils of 10μm (—●—●—), 50μm (—○—○—), 200μm (--●--●--) and 1000μm (--○--○--) thickness.

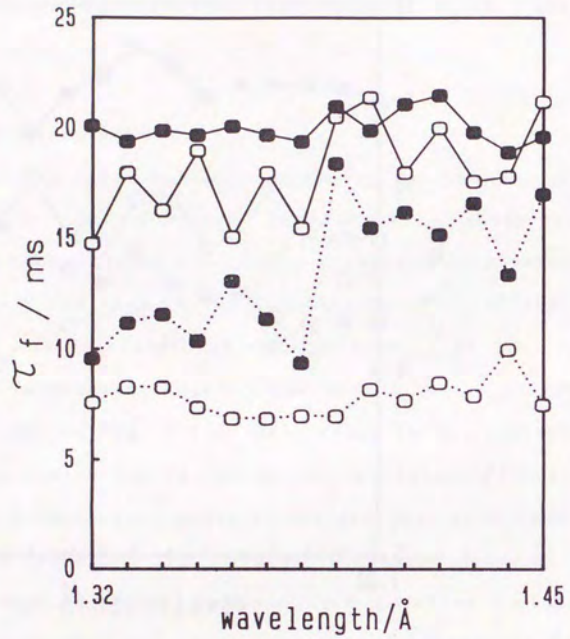

Fig. 3-4-2 Dependence of τ_f on X-ray wavelength for copper foils of 10 μm (—●—● —), 50 μm (—○—○—), 200 μm (--●---●--) and 1000 μm (--○---○--) thickness.

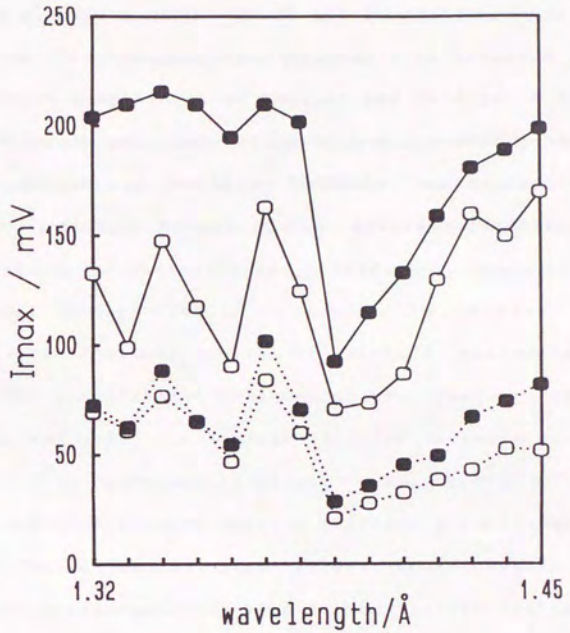

Fig. 3-4-3 Dependence of I_{max} on X-ray wavelength for copper foils of 10 μm (—●—● —), 50 μm (—○—○—), 200 μm (--●---●--) and 1000 μm (--○---○--) thickness.

to that of EXAFS (10 to 80eV) reported in literatures[39,40], and the amplitude of the fluctuations are large compared to that measured by a conventional photoacoustic measurement[41] where X-ray beam was chopped by an ordinary regular chopping sector. However, a possibility that the periodic change is some reflection of EXAFS could not be denied absolutely. Further investigation will be needed in this point.

CHAPTER IV

Simultaneous Measurement of X-ray Photoacoustic and Fluorescence Signals

Simultaneous photoacoustic and fluorescence measurement has been conducted in the X-ray region. The simultaneous measurement provides the means of non-destructive characterization of materials and provide an understanding of the total energy flow in a sample. In section 4-1, application to characterization of layered materials is discussed. The simultaneous measurement was conducted on the metal foils and model samples with layered structures. In section 4-2, an approach to direct measurements of the absolute X-ray fluorescence quantum efficiency is discussed. New method based on the simultaneous photoacoustic and fluorescence measurement was used in the visible region in this section. In section 4-3, the first attempt of this method in the X-ray region is described.

Sections 4-1, 4-2 and 4-3 are base on previously published reports[38,42-44].

4-1 Simultaneous Detection of X-ray Photoacoustic and Fluorescence Signals as Applied to Characterization of Layered Materials

Introduction

The X-ray fluorescence method is advantageous since it is a non-destructive elemental analysis technique that is convenient, while the results of measurement are strongly dependent on the state of the specimen. Photoacoustic measurement combined with X-ray fluorescence measurement provides information concerning the amount of net absorption, thermal and geometrical properties of layered materials. Furthermore, a comparison of the X-ray, visible and UV wavelength regions is of interest, since the samples have different absorption properties from the ordinary UV and visible wavelength regions in the X-ray region.

Experimental

A built-in type X-ray tube with a molybdenum target was used as the excitation source. Figure 4-1-1 is a schematic diagram of the experimental setup. The X-ray beam was narrowed and collimated by the molybdenum collimator with a diameter of 1mm. A molybdenum spinning rod (R) with a bored hole was used to chop the excitation beam. The body of the photoacoustic cell was made of brass, and the windows and

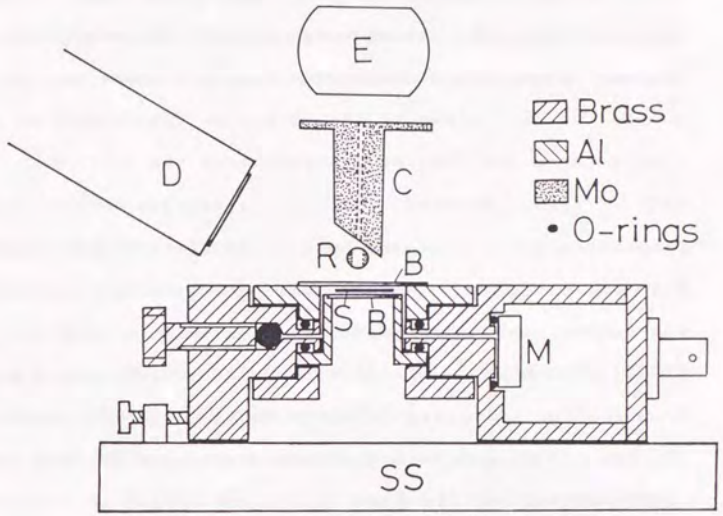

Fig. 4-1-1. A sectional view of the experimental arrangement for simultaneous X-ray photoacoustic and fluorescence measurement.
S, Sample; B, Be window; M, microphone; D, Si(Li) detector; E, Mo target X-ray tube; C, 1mm collimator; R, rotating rod chopper; SS, sliding stage.

their frames were made of beryllium and aluminum, respectively. The thicknesses of the windows were 0.5mm (upper) and 0.25mm (lower). The sample chamber was designed so as to be close to the detector in order to avoid fluorescence and scattered X-rays from the cell wall. The cell was mounted on a sliding stage. X-ray fluorescence was detected by a solid state Si(Li) detector. The photoacoustic signal was detected by a condenser microphone and then amplified by a lock-in amplifier (NF CIRCUIT BLOCK INC., LI574A with P-51A preamplifier) and read by a digital voltmeter (HEWLETT PACKARD, 3456A). In the case of the photoacoustic measurement involving UV and visible light excitation, the upper beryllium window of the cell was replaced with a quartz window of 1mm thickness; the light beam from a 500W xenon arc lamp was filtered and focused to a spot of about 5mm diameter on the specimen. For UV light excitation, a UV transmission filter (TOSHIBA, UVD-33B) and an IR cut filter (TOSHIBA, IRA-25S) were used. In the visible region a UV cut filter (TOSHIBA, Y44) and an IR cut filter (TOSHIBA, IRA-25S) were used. Sheets of copper foils (thickness 10μm to 1mm and diameter 10 to 18mm), laminated sheets of copper foils (thickness 100μm, diameter 18mm) and adhesive tapes (thickness about 50μm), and laminated sheets of lead foils (thickness 100μm, diameter 18mm) and aluminum foils (thickness about 15μm, diameter 18mm) were used as

samples. Copper foils were polished and stored in ethanol. In the case of the laminated specimens, polymer adhesive tape or aluminum foil was adhered to both sides of the copper or lead foil.

Results and Discussion

Photoacoustic and fluorescence signals were simultaneously detected at an X-ray tube voltage of 40KV and 20mA. The fluorescence signal, however, was very strong and the dead time of the Si(Li) detector approached 90% under these conditions; thus, the X-ray tube current was reduced to 2mA when fluorescent measurements alone were performed. Figure 4-1-2 shows the change in the X-ray photoacoustic and fluorescence (Cu K_α) signal intensity plotted as a function of the copper foil thickness. The visible photoacoustic signal intensity for the same specimens are also plotted in Fig. 4-1-2. A chopping frequency of 8Hz was used for both measurements. The fluorescence signal intensity is constant, except for the 10μm thick specimen. Since the X-ray fluorescence critical thickness is about 30μm for copper[45] (excitation Mo K_α, incidental angle 90°, detection angle 30° I/I_∞ =0.99), the fluorescence signal is considered to be independent of the thickness for thickness greater than 30μm. On the other hand, both the X-ray and visible photoacoustic signal intensities depend on the specimen

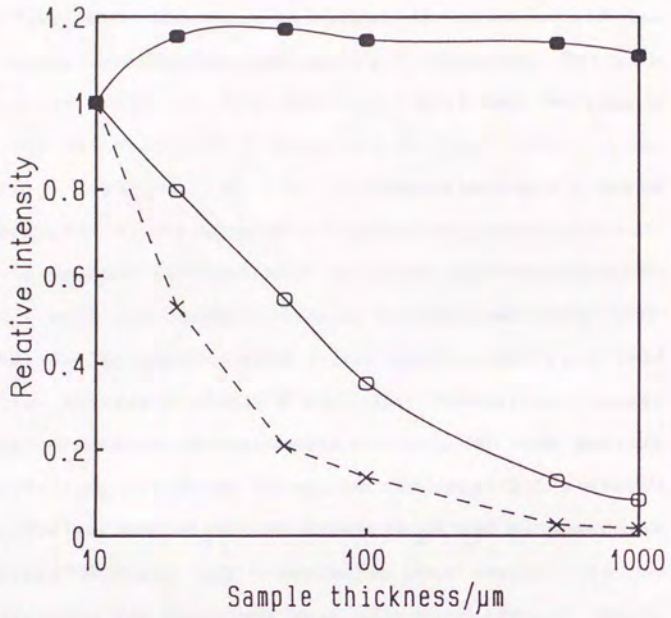

Fig. 4-1-2. Photoacoustic and fluorescence signal intensities for different copper foil thicknesses.
—○—○— :X-ray photoacoustic signal,
···×···×·· :visible photoacoustic signal,
—●—●— :X-ray fluorescence signal.

thickness. The reason for the decrease in the photoacoustic intensity with increasing film thickness is considered to be due to heat diffusion in the specimen. The thermal diffusion length for copper at a chopping frequency of 8Hz is about 2.2mm, which is thicker than the specimen thickness. Thus, the heat generated by X-ray absorption was considered to be uniformly spread throughout the specimen. Under these conditions, the X-ray photoacoustic signal intensity, P, for a copper foil was estimated to be:

$$I(E) = k\, I_o(E)\, \{ 1 - \exp(-t\, \mu(E)\, \rho) \} / t \qquad (4.1.1)$$

and

$$P = \Sigma\, I(E), \qquad (4.1.2)$$

where $I(E)$, k, $I_o(E)$, $\mu(E)$, ρ and E are the photoacoustic signal intensity, an instrumental constant, the initial X-ray beam intensity, the mass absorption coefficient of the specimen, density of the specimen, and the photon energy of the incident beam, respectively. The mass absorption coefficient, μ, is generally given by[1]:

$$\mu(E) = \tau(E) + \sigma(E) \qquad (4.1.3)$$

and

$$\tau(E) = C\, E^{-3} - D\, E^{-4}, \qquad (4.1.4)$$

where $\tau(E)$ and $\sigma(E)$ are the photoelectric absorption and the scattering loss of the X-ray beam respectively. In photoacoustic measurements, only τ contributes to the photoacoustic signal generation. Parameters C and D are

functions of the atomic number. Figure 4-1-3 is a log-log plot of the photoacoustic signal intensity versus the thickness of the specimen. Estimated values of the X-ray photoacoustic signal intensity were calculated using equations (4.1.1)-(4.1.4) with the energy distribution of X-ray source in the range 0.5 to 40.5 KeV. The energy distribution of the X-ray source was measured by an Si:Li detector attached to the X-ray fluorescence apparatus using an acrylic resin plate (thickness 10mm) as a diffuser. The visible photoacoustic signal intensity was found to be inversely proportional to the thickness. Visible light was absorbed at the surface of the specimen and the amount of absorbed energy was independent of the specimen thickness. Thus, the temperature change was inversely proportional to the heat capacity which, in turn, was proportional to the thickness of the specimen. This supports one of the assumptions that the heat generated in a specimen is spread uniformly within the specimen. The X-ray photoacoustic signal intensity for thin specimens showed a tendency to approach a constant value, which is in agreement with the calculated curve. On the other hand, a decrease in the X-ray photoacoustic signal intensity for thick specimens was found to be smaller than the estimated value. The discrepancy between the experimental value and the estimated value was small and is interpreted in terms of the heat loss by

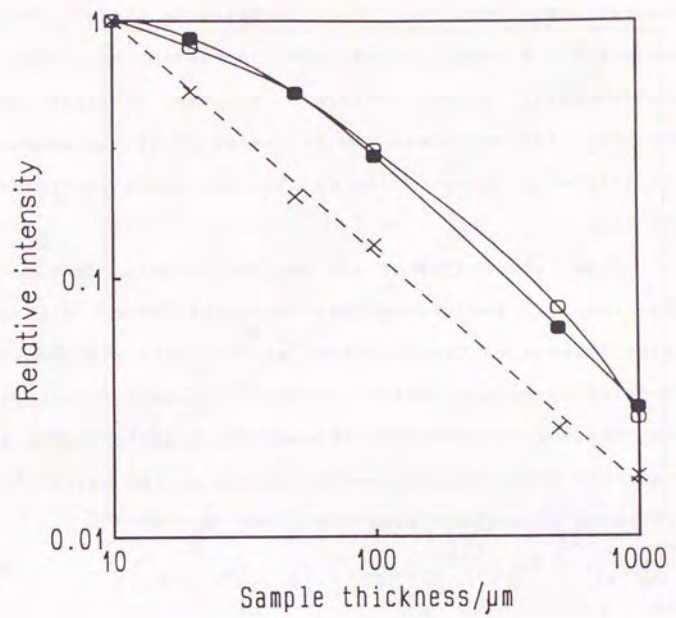

Fig. 4-1-3. Log-log plots of photoacoustic signal intensity for different copper foil thicknesses.
Photoacoustic signal intensities estimated from the mass absorption coefficient and the heat capacity are also plotted.
—○—○— :X-ray photoacoustic signal,
--×---×-- :visible photoacoustic signal,
—●—●— :estimated X-ray photoacoustic signal.

fluorescence, and by the background signal caused by scattered X-rays. Since the intensity of the X-ray photoacoustic signal depends on the thickness of the specimen, the thickness can be estimated if the component of the sample is known or the calibration curve was previously obtained.

When absorption of the excitation beam occurs within the sample, the photoacoustic signal shows a phase lag which depends on the thickness of the coating layer and the chopping frequency. This is because any heat generated under the coating is conducted through the coating layer, and is converted into a photoacoustic signal at the surface[6]. The following equations give the phase lag, ϕ:

$$\phi = t\,(2\alpha)^{-1/2}\,\omega^{1/2} + C, \qquad (4.1.5)$$

and

$$\alpha = k / (c\,\rho), \qquad (4.1.6)$$

where ϕ, t, α, ω, C, k, ρ and c are the phase lag, the sample thickness, the thermal diffusivity of the sample, the angular chopping frequency, constant, the thermal conductivity of the sample, the density of the sample, and the heat capacity of the sample, respectively. Figure 4-1-4 shows the phase lag of the photoacoustic signal for a laminated sample of copper foil and polymer sheets for various excitation sources. The phase lag shows a linear relation with the square root of the chopping frequency.

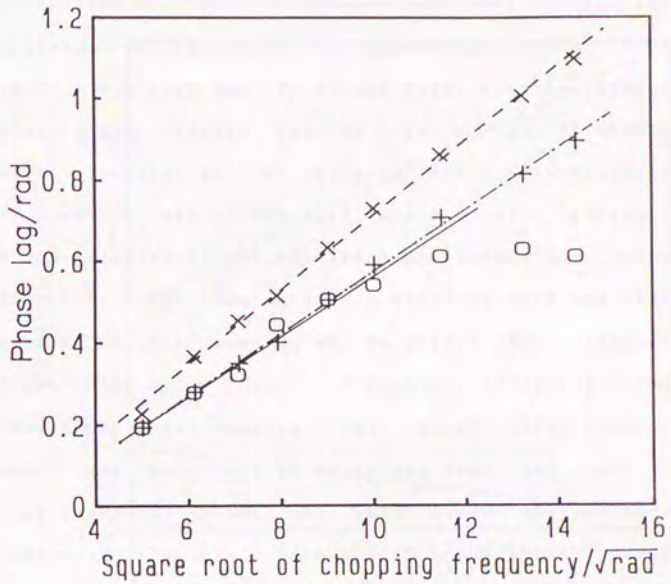

Fig. 4-1-4. Phase lag of the photoacoustic signal *versus* the square root of the angular chopping frequency for a laminated specimen of copper foil and polymer film.

—○—○— :X-ray photoacoustic signal,

--×--×-- :visible photoacoustic signal,

-·+-·+- :UV photoacoustic signal.

The polymer layer was transparent for all excitation beams used in this experiment. The slopes of the regression line determined by a least-square fitting were 0.073, 0.076, and $0.092 s^{1/2}$ for X-ray, UV and visible light excitation, respectively. The density of the polymer layer was $1.33 g/cm^3$. If the heat capacity of the polymer layer is known, the thermal conductivity can be calculated. Assuming that the heat capacity of the polymer layer is $2 Jg^{-1}K^{-1}$, the thermal conductivity of the polymer layer is calculated to be 3.9×10^{-3}, 5.8×10^{-3}, and $6.2 \times 10^{-3} Jcm^{-1}s^{-1}K^{-1}$, respectively. Since the polymer layer absorbed UV and X-rays, the heat generated by absorbing the beam near the surface would make the phase lag small for UV and X-ray excitation. On the other hand, the phase lag for a laminated specimen of lead foil and aluminum foil (Fig. 4-1-5) exhibits somewhat different behavior. Since aluminum is transparent to X-rays, the phase lag increased proportionally to the square root of the chopping frequency. On the other hand, aluminum is opaque to visible light; thus, that phase lag is constant for the chopping frequency. The slope of the regression line determined by least-square fitting for an X-ray photoacoustic signal was $0.019 s^{1/2}$. This value is large compared to the estimated value ($1.2 \times 10^{-3} s^{1/2}$) from the thickness ($15 \mu m$), the thermal conductivity ($2.04 Jcm^{-1}s^{-1}deg^{-1}$), the density

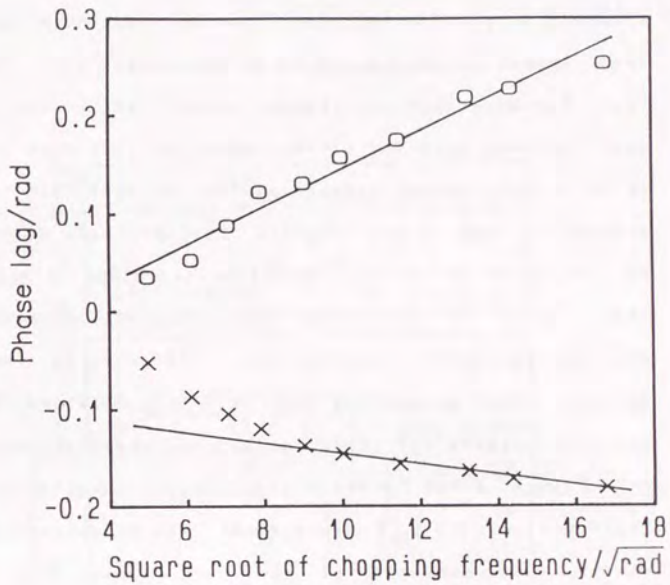

Fig. 4-1-5. Phase lag of the photoacoustic signal *versus* the square root of the angular chopping frequency for a laminated specimen of lead foil and aluminum foil.

—○—○— :X-ray photoacoustic signal,

—×—×— :visible photoacoustic signal.

($2.69 g/cm^3$) and the heat capacity ($0.895 Jg^{-1}deg^{-1}$) of the aluminum layer. The adhesive layer between the aluminum and lead layers is considered to be the reason for the phase lag. Assuming that the thermal conductivity, the density, and the heat capacity of the adhesive layer were equal to those of poly-methacrylate resin[20] ($1.5 \times 10^{-3} Jcm^{-1}s^{-1}deg^{-1}$, $1.2 g/cm^3$, and $1.4 Jg^{-1}deg^{-1}$), the thickness of the layer was estimated to be about 8μm from the slope ($0.019 s^{1/2}$). This value is consistent with values determined by microphotographic observations. Information concerning surface layer properties can, thus, be obtained from the relation between the phase lag and the chopping frequency.

Figure 4-1-6 shows a simultaneous photoacoustic and fluorescence (Pb L_α) measurement. The fluorescence signal shows the presence of the lead layer (Fig. 4-1-7). Characteristic X-ray fluorescence peaks were observed at X = 4 and X = 10mm. The X-ray and visible photoacoustic signals indicate that the X-ray absorption coefficient of the inner layer at the center of the specimen (X = 7mm) is low, and that the heat conductivity of the inner layer is lower than that for lead. The phase lag of the photoacoustic signal by visible light excitation exhibits a small deviation. This indicates that the absorption of visible light occurs at the surface layer of the specimen. On the other hand, the phase lag by X-ray excitation showed a large deviation, which

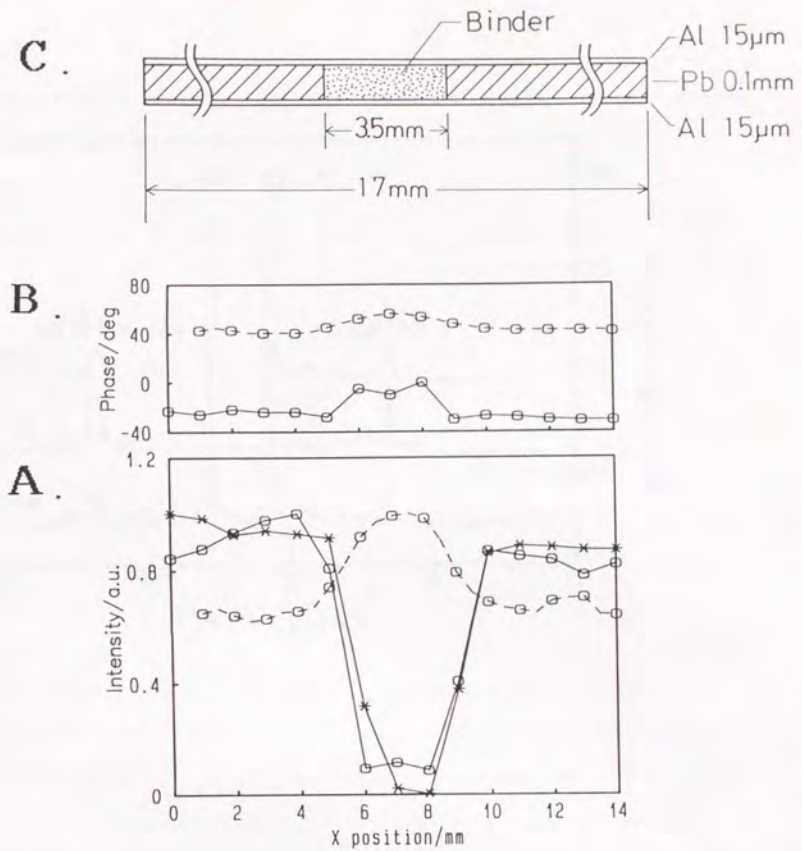

Fig. 4-1-6. Simultaneously measured photoacoustic and fluorescence signals (A) by X-ray excitation for a model specimen (C). The photoacoustic signal for the same specimen excited by visible light is also plotted. The upper traces (B) show the photoacoustic signals phase lags.

—○—○— :X-ray photoacoustic signal,

···○···○··· :visible photoacoustic signal,

—×—×— :X-ray fluorescence signal.

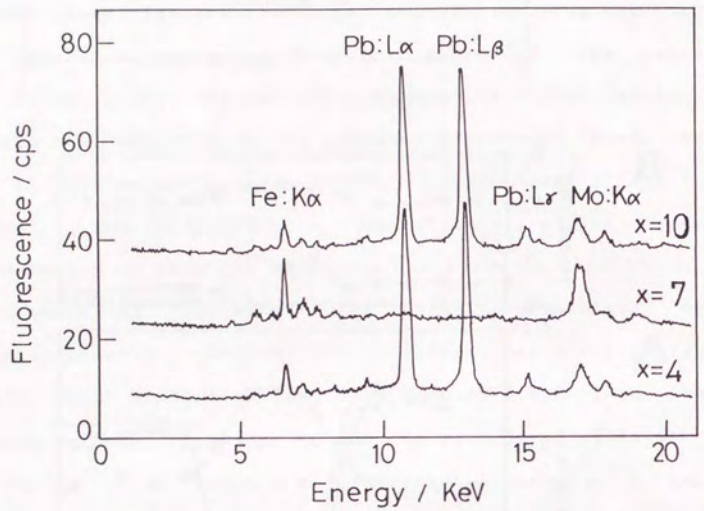

Fig. 4-1-7. Fluorescence spectra simultaneously measured with the photoacoustic signal at position X = 4, 7, 10mm.

indicates a change in the average depth where X-ray absorption occurred.

4-2 An Approach to the direct Measurement of the Absolute X-ray Fluorescence Quantum Yield (Simultaneous Measurement of Photoacoustic and Excitation Spectra for the Evaluation of Fluorescence Quantum Yields of Uranium-mica Type Compounds)

Introduction

We have developed and reported a new method for measuring the absolute fluorescence quantum yield. Although, this method was performed in the visible region, it could be applied to X-ray region. In the next section the first attempt of this method in the X-ray region will be described.

The determination of the absolute quantum yield of fluorescence may be achieved either by determination of a defined fraction of the fluorescent radiation, or by measurement of the complementary part of the non-radiative process by calorimetry[46]. The former optical method appears to be more popular. Electronic units and components are also readily available. But, it is known that absolute measurements of fluorescence quantum yield are difficult to perform experimentally[3,47,48]. The actual determination of quantum yield consists of various processes.

The photoacoustic technique enables measurement of the absolute fluorescence quantum yield in the visible light

region[49-52]. In these studies, measurement of the fluorescence quantum yield are based on two phenomena. The first is that the fluorescence can be quenched by a quencher. And the second is that the fluorescent life time is longer than the non-fluorescent transition life time. Lahmann and Ludewig[53] compared the photoacoustic signal of a sample solution of rhodamine 6G with that of $K_2Cr_2O_7$ as a reference which is nonfluorescent but has comparable absorption coefficients. Adams *et al.*[49] determined the quantum yield of quinine bisulfate in aqueous solution utilizing the quenching effect of fluorescence by halide ions. Fluorescence quantum yield was obtained from a ratio of the photoacoustic signal intensities before and after quenching with the use of a quencher. In the case where the fluorescent life time is long, it was found that the photoacoustic signal measured at high chopping frequencies is dependent only on the energy released in the non-radiative transition[52]. Theoretically, however, there is no quencher for X-ray fluorescence and the fluorescent life time is extremely short in the X-ray region. Therefore, these methods are not useful in the X-ray region. We have developed a new method to measure the absolute fluorescence quantum yield without the use of quenchers. This method is based on simultaneous detection of the photoacoustic and excitation signals as a function of the excitation

wavelength.

Experimental

The experimental system used for the simultaneous measurement of photoacoustic and fluorescence spectra is shown in Fig. 4-2-1, where the system for measuring luminescence life time is also shown. The light used for excitation is a xenon lamp (300W) chopped (CH1) at 80Hz and monochromated at SP1 (JASCO, CT25N) and irradiated on the sample cell (PFC). The cross section of the cell is shown in Fig. 4-2-2, and the details were reported in elsewhere[42]. The Photoacoustic signal is detected by a microphone (SONY, Electret condenser type, FET buffer included, parts number 8-814-196-50) attached to the cell, amplified at P1, introduced to lock-in amplifier L2 (NF Circuit Block LI-574) and recorded at R2. The optical signal is monochromated at SP2, detected by a photomultiplier (PM), amplified (P3 and L1) and recorded at R1.

In the fluorescence emission measurements, the sample is irradiated with UV light (365nm) from a mercury lamp (HgL) and the fluorescent emission is monochromated by monochromator SP2 (NIKON, P-250), chopped (CH2), and detected by photomultiplier PM. With the luminescence life time measurements, the sample specimen is placed at the S2 position instead of the S1 position and, is excited by a

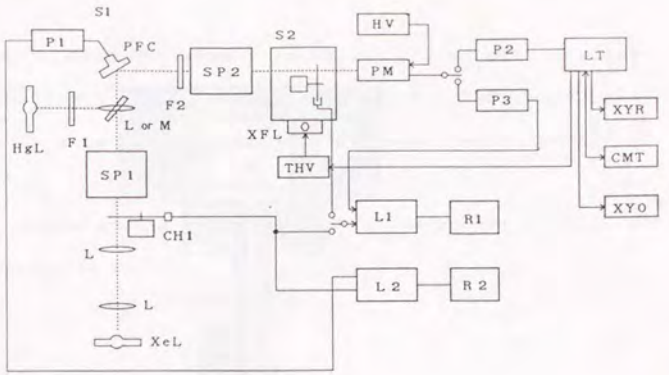

Fig. 4-2-1. Block diagram showing the system for simultaneous photoacoustic and fluorescent measurements. The system for measuring fluorescent life time is also shown.
XeL, Xenon arc lamp; L, lenses; CH1 and CH2, light choppers; HgL, mercury lamp, F1 and F2, filters; PFC, sample cell; S1 and S2, sample positions; THV, trigger circuit and power supply for xenon flash lamp XFL, xenon flash lamp; PM, photomultiplier; P1, P2 and P2, preamplifiers; L1 and L2, lock-in amplifiers; R1 and R2, recorders; LT, signal processor unit with microcomputer; XYR, XY-recorder; CMT, magnetic tape recorder; XYO, XY-oscilloscope, SP1 and SP2, monochromators.

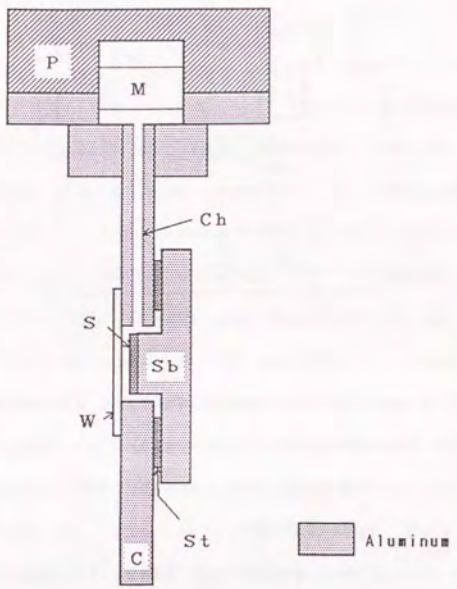

Fig. 4-2-2. Sample cell for simultaneous photoacoustic and fluorescence measurements.
S, sample; W, quartz window; St, sticky packing; Sb, sample base; Ch, channel; M, microphone; P, acoustic protective cover; C, aluminum cell body.

xenon flash lamp XFL. The fluorescent signal is detected (PM), amplified (P2), and introduced to the life time measuring system LT, the details of which were published elsewhere[54].

All measurements in the present study were taken at room temperature.

Samples.

The samples used in the present study were prepared according to the literatures[55,56]. The general formula of the uranium-micas are given[57] as $M(UO_2)_2(XO_4)_2 \cdot nH_2O$, where M is a univalent metal ion $M^{+}{}_2$ or a bivalent metal ion M^{2+}, and XO_4 is a phosphate PO_4^{3-} or arsenate AsO_4^{3-} anion. The prepared samples are those with M = $(H_3O)_2$, Na_2, K_2, Mg, Ca, Sr, Ba, Zn. The number of water molecules *n* varies according to the condition of the sample; natural autunites with bivalent metal ions have values of *n* ranging from 8 to 12, while those with univalent ions have, to some extent, a lower value of *n*. Fluorescence spectra and fluorescence life time of those samples were also measured and discussed in a previous report[58].

Results and Discussion

Procedure for Determining the Fluorescence Quantum Yield

In a system which is not chemically reactive to visible

light irradiation, photoacoustic spectrometry provides a complementary system to fluorescent spectrometry which deals with radiative processes. A method of estimating the absolute quantum yield of fluorescence Q_F is presented in Fig. 4-2-3. This is based on a simple model where the ground state G and the excited state B of a broad band is given with separation ΔE. Assuming the system absorbs light energy E larger than ΔE, the system will release the heat energy and will return to the bottom of the band, from which the system will relax to the ground state G by either radiative (F) and/or non-radiative (N) transition. The intensity of the fluorescent emission $I_f(E)$ caused by excitation of light with energy E is given by

$$I_F(E) = k\ \beta(E)\ Q_F\ I_{EX}(E), \qquad (4.2.1)$$

where k is a measuring constant, $\beta(E)$ is the absorption coefficient for the light energy E, and $I_{EX}(E)$ is the intensity of the excitation light at energy E. The photoacoustic signal is proportional to the output of the thermal energy, which is given as the sum of the excess energy, $E - \Delta E$, and the energy released in the non-radiative process N. Thus the photoacoustic intensity $I_P(E)$ is given by

$$\begin{aligned} I_P(E) &= I\ \beta(E)\ I_{EX}(E)\ [E - \Delta(E) + \Delta E(1 - Q_F)] \\ &= I\ \beta(E)\ I_{EX}(E)\ (E - \Delta E\ Q_F), \end{aligned} \qquad (4.2.2)$$

where I is a measuring constant. By using that $\beta(E)$ and

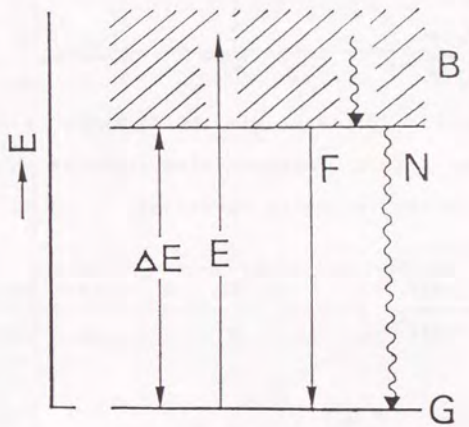

Fig. 4-2-3. An energy diagram tentatively given for deriving the relations in the fluorescence quantum yield calculation. F denotes a radiative process while N denotes a non-radiative process.

$I_{EX}(E)$ are taken as constants, $I_F(E)$ and $I_P(E)$ will be given as functions of energy E as shown in Fig. 4-2-4. By taking the ratio of $I_P(E) / I_F(E)$, the $\beta(E)$ and $I_{EX}(E)$ terms vanish giving:

$$\frac{I_P(E)}{I_F(E)} = \frac{1}{k} \frac{E - \Delta E \quad Q_F}{Q_F} \qquad (4.2.3)$$

The $I_P(E) / I_F(E)$ ratio will be directly related to E as shown in Fig. 4-2-4c. Extrapolation leads to an energy of E_o as shown in the following equations;

$$\frac{I_P(E)}{I_F(E)} = 0 = \frac{1}{k} \frac{E - \Delta E \quad Q_F}{Q_F} \qquad (4.2.4)$$

i. e.,

$$E_o = \Delta E \; Q_F \qquad (4.2.5)$$

The quantum yield is then given by

$$Q_F = E_o / \Delta E. \qquad (4.2.6)$$

Experimentally, the E_o value is obtained as a crossing point on the E axis in the extrapolation of the plots of $I_P(E) / I_F(E)$ *versus* E, and the ΔE value will be obtained as the center of the gravity of the emission spectra.

The method for estimating the quantum yield presented here represents an improvement of those reported to date[49, 53] in that reference materials and quenched samples are not required. In addition, simultaneous measurement followed by plotting the intensity ratio of both spectra

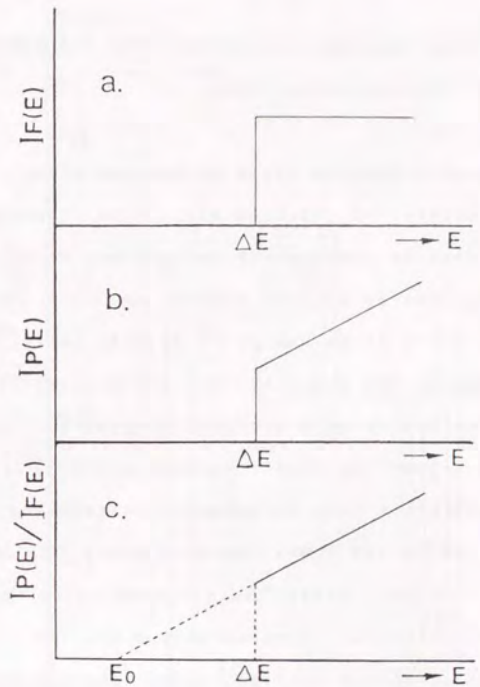

Fig. 4-2-4. Expected intensities of fluorescent (a) and photoacoustic (b) outputs based on diagram Fig. 4-2-3, and their ratio (c) as a function of excitation energy E.

removes the need for corrections for the power spectrum and drift of the excitation light.

Fluorescence Quantum Yield of Uranium-micas.

A series of uranium-mica type compounds containing uranyl ions as fluorescent centers may be considered as one with an energy diagram similar to that discussed above. Figure 4-2-5 is an energy level diagram for the uranyl(VI) ion base on the paper by Bell and Biggers[59] which appears to be the most widely accepted diagram for uranyl salts. The totally symmetric singlet ground state $^1\Sigma^+_g$ is split into five sublevels due to symmetric stretching in the ground state, while the lowest excited state $^3\Pi_u$ and the second lowest excites state $^3\Delta_u$ are also split into twelve and seven sublevels, respectively, due to the symmetric stretching in the excited state. The average spacings of the sublevels are approximately 750-860cm^{-1} depending on the respective sample[60-62]. The luminescence appears to occur from the lowest one or two sublevels to the ground state sublevels showing six emission peaks. The emission peak at the shortest wavelength has a relatively small intensity of about 1/30 of the total intensity suggesting that the contribution to the emission from the second lowest sublevel is negligibly small.

The emission spectra of $Ba(UO_2)_2(PO_4)_2 \cdot nH_2O$, one of

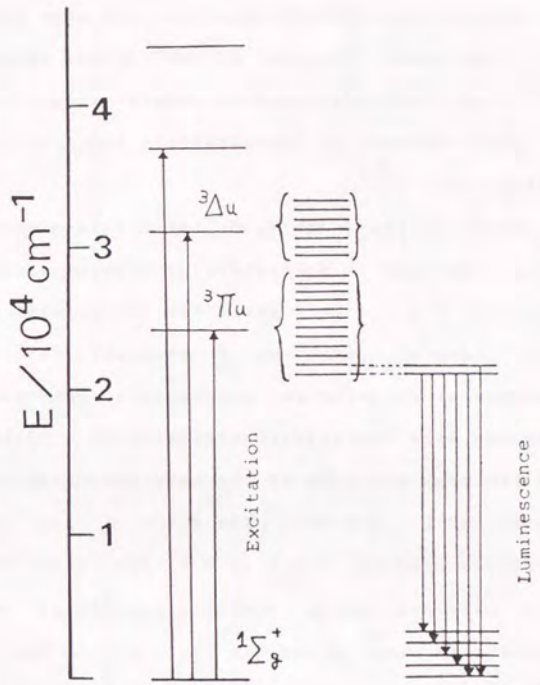

Fig. 4-2-5. Energy level diagram showing the excitation and fluorescent transitions for a uranyl(VI) ion[9].

the prepared uranium-mica samples, are also shown in Fig. 4-2-6. The main features of the three spectra are very similar to other uranium-mica samples except for shifts from the peak values of approximately 5nm in the respective spectra.

Plots of the $I_F(E) / I_F(E)$ ratio *versus* excitation energy E for the case of Ba-containing uranium-mica samples are given in Fig. 4-2-7, where the six points in the lower energy region fall on a straight line giving the experimental E_o value on the abscissa. The experimental ΔE value has been tentatively evaluated as $1.92 \times 10^4 cm^{-1}$ (520nm) from the peak position of the envelope curve of the emission spectra (Fig. 4-2-6a). The value of the quantum yield, calculated from Eq. 4.2.6 is 0.7. The value of the quantum yield obtained using similar procedures for the other uranium-mica are given in Table 4-2-1. The E_o value of 1.92×10^4 cm^{-1} has been constantly applied in the estimation of quantum yields of other uranium-micas. The error from this approximation is estimated to be $\pm 4\%$. Table 4-2-1 includes the fluorescence life times and the transition rate constants which will be discussed later.

In Fig. 4-2-7, some of the data in the higher energy region deviate from linearity. This deviation was also found in other uranium-micas, where the number of points falling on the line ranges from 4 to 7 out of fifteen.

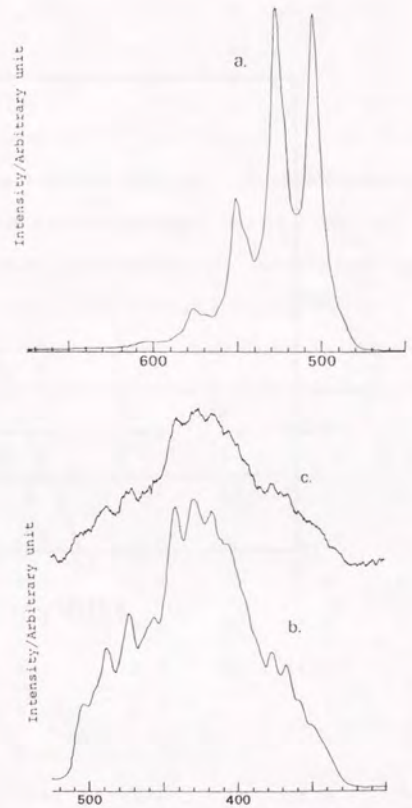

Fig. 4-2-6. Fluorescent emission spectra (a), fluorescent excitation spectra (b) and photoacoustic spectra (c) of $Ba(UO_2)_2(PO_4)_2$ nH_2O. The latter two spectra were measured simultaneously.

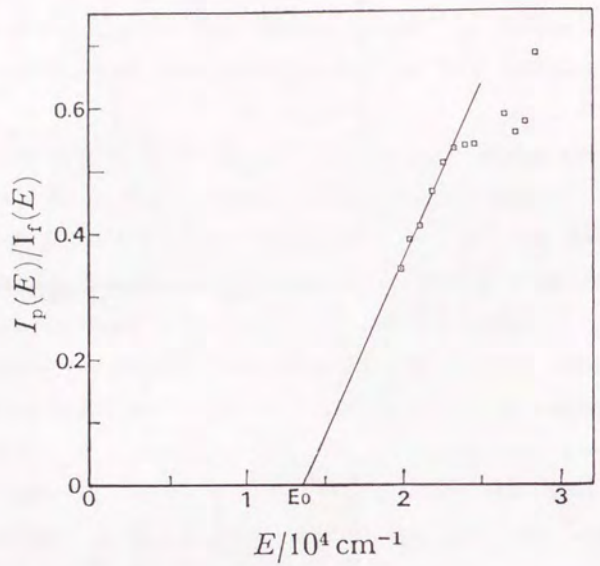

Fig. 4-2-7. Plots of the intensity ratios of photoacoustic and fluorescent excitation signal intensities as a function of excitation energy E.

Table 4-2-1. Data of quantum yield Q_r, fluorescence life time τ, and transition rate constants k_f and k_n of the respective radiative and non-radiative processes for a series of uranium-mica compounds $M(UO_2)_2(XO_4)_2 \cdot H_2O$.

	X = P				X = As			
M	Q_r	τ	k_f	k_n	Q_r	τ	k_f	k_n
	%	10^{-4}s	$10^{-3}s^{-1}$	10^3s^{-1}	%	10^{-4}s	$10^{-3}s^{-1}$	10^3s^{-1}
$(H_3O)_2$	0	-	0	-	72	1.4*	5.1*	2.0*
Na_2	86*	2.4	3.6*	0.6*	90	0.82	12.0	1.2
K_2	86	2.8	3.1	0.5	79*	1.0*	7.9*	2.1*
Mg	86	2.8	3.1	0.5	92	1.2	7.7	0.7
Mg:Mn	58	1.7	3.4	2.5	Mn:0.03mol%			
Ca	78*	2.6	3.0*	0.8*	-	1.4*	-	-
Sr	75*	3.4	2.2*	0.7*				
Ba	70	2.8	2.5	1.0	73	1.9	3.9	1.3
Zn:Cu	75*	1.4*	5.4*	1.8*	Cu:0.01mol%			
Zn:Cu	10	1.6*	0.6*	5.6*	Cu:0.1mol%			

* less reliable data.

The reason for the observed deviation appears to be due to the grain size δ of the sample powder. For a photoacoustic signal P_m for a solid sample[7,63], P_m varies as a rather complex function of the sample parameters and/or experimental conditions such as absorption coefficient β, thermal conductivity, grain size δ and the optical penetration distance, μ, which is defined as $1/\beta$, appears to be responsible for the deviation.

In the situation where μ is larger than δ, the acoustic signal P_m is proportional to β, whereas if μ is comparable to or smaller than δ, the acoustic signal P_m remains constant and independent of β. This indicates that in the energy region of 400-450nm (relatively large β, the optical penetration distance μ is equal to or smaller than δ, so that the intensity of the photoacoustic signal will be reduced to some extent, resulting in deviation from linearity. The plots in the higher energy region appear closes to the line than those in the intermediate energy region which appears to correspond to a lower β value in this region. Samples having a large grain size such as $Mg(UO_2)_2 \pm nH_2O$:Cu (0.01mol%) do not show deviations. It may be concluded that a sample with a smaller grain size gives greater linearity and thus more reliable results in terms of estimation of the quantum yield.

Transition Rate Constants k_f and k_n for the Radiative and Non-radiative Process.

The combination of the values of quantum yield Q_F and the fluorescence life time allows the transition rate k_f for the radiative process and k_n for the non-radiative process to be evaluated. The values are related by the following equation;

$$\tau = 1 / (k_f + k_n) \qquad (4.2.7)$$

$$Q_F = k_f / (k_f + k_n), \qquad (4.2.8)$$

which may be rewritten:

$$k_f = Q_F / \tau \qquad (4.2.9)$$

$$k_n = (1 - Q_F) / \tau. \qquad (4.2.10)$$

The results calculated from Eqns. 4.2.9 and 4.2.10 are given in Table 4-2-1. The life time data in Table 4-2-1 have been measured in this study, and are slightly different from those previously reported[58]. The difference is considered to be within experimental error as far as room temperature data are concerned. As can be seen in Table 4-2-1, the phosphate samples have Q_F, k_f, and k_n values of approximately 80%. $3 \times 10^3 s^{-1}$, and $0.5\text{-}1.0 \times 10^3 s^{-1}$ respectively. The arsenate samples have a shorter τ, a slightly larger Q_F, and a larger k_f value than in the phosphate samples. The k_n values are comparable for the phosphate and arsenate samples. This suggests that the fast radiative process (large k_f) makes the life time short for samples without quencher ions such

as Cr and Mn. Samples with quencher ion $Mg(UO_2)_2(PO_4)_2 \pm nH_2O$:Mn (0.03mol%), however, have a shorter τ and lower Q_{FL} leading to a larger value of k_n. It is considered that the effect of the doping ion Mn^{2+} receives part of the excited energy of the UO_2^{2+} ion making the τ value shorter as well as making the Q_F value lower. The effect of the doping Cu^{2+} ions absorb nearly all the excited energy of the nearest UO_2^{2+} ions causes the Q_F to decrease, while the other UO_2^{2+} ions which are free from Cu^{2+} neighbors decay by their own relaxation mechanism.

4-3 Simultaneous Detection of X-ray Photoacoustic and Fluorescence Signals for Evaluation of Fluorescence Quantum Yield

Introduction

Photoacoustic spectroscopy is based on the measurement of heat generation subsequent to alternating excitation. Since the heat is related to non-radiative decay process, photoacoustic spectroscopy combined with fluorescence spectroscopy enables one to trace the total flow of the relaxed energy passing through both radiative and non-radiative processes. We have reported that the fluorescence quantum yield can be determined by analyzing the spectra measured simultaneously[42,43]. Although, the analysis was conducted in the visible region, one can also apply this technique to the X-ray region. We have reported on making a photoacoustic cell for simultaneous photoacoustic and fluorescence measurements in the X-ray region[38]. In this study simultaneous measurements were attempted with use of a monochromatic X-ray source for evaluation of the fluorescence quantum yield.

Theoretical

Theories presented in section 4-2 are modified so as to apply to X-ray fluorescence. A system which has a ground

state and a continuous band of excited states, with energy gap E_{ab} between them is assumed. The system absorbs photons with energy higher than E_{ab} and relaxes to the ground state through radiative and nonradiative processes. In the X-ray region, the former is fluorescence radiation and the latter involve Auger electron emission. These electrons are trapped in the surrounding air or sample itself and generate heat. The intensity of the fluorescence signal $I_{fn}(E)$ (n=1, 2, 3...) and photoacoustic signal $I_p(E)$ for an excitation with intensity I_o and photon energy E is given as,

$$I_{fn}(E) = C_1 \; I_o(E) \; \beta(E) \; Q_{fn},$$

$$I_p(E) = C_2 \; I_o(E) \; \beta(E) \; [\; E - \Sigma \; \Delta E_n \; Q_{fn} \;],$$

where $\beta(E)$, Q_f, ΔE_n and $C_{1,2}$ is the absorption coefficient, the quantum yield of n-th fluorescence, energy of n-th fluorescence and experimental constant respectively. Taking the ratio I_p / I_{fm} (m=1, 2, 3...), the β and I_o terms vanish thus giving:

$$\frac{I_p(E)}{I_{fm}(E)} = \frac{C_2}{C_1} \quad \frac{E - \Sigma \; \Delta E_n \; Q_{fn}}{Q_{fm}} .$$

If we plot the experimental $I_p(E) / I_{fm}(E)$ value with respect to E, and extrapolate the plotted line to the point where it crosses the E axis, we will obtain E_{om}. With this value, one obtain the fluorescence quantum yield as follows,

$$E_{om} - \Delta E_m \; \Sigma \; Q_{fn} = 0$$

$$Q_{fm} = E_{om} \; / \; \Delta E_m \; (\; \Delta E_m \; Q_{fm} \; / \; \Sigma \; \Delta E_n \; Q_{fn} \;).$$

Value of $\Delta E_m \; Q_{fm} \; / \; \Sigma \; \Delta E_n \; Q_{fn}$ can be obtained experimentally from intensity ratio and energy of fluorescence X-rays.

Experimental

The experiment was conducted at beam line BL-4A at the Photon Factory (National Laboratory for High Energy Physics, KEK, Tsukuba). A chopped X-ray beam (20Hz) was irradiated onto a sample placed in a photoacoustic cell. The photon energy of the incident X-ray was in the 8 to 14 KeV region. The experimental set up is shown in Fig. 4-3-1. The windows and frames of the cell are made of beryllium and aluminum, respectively. X-ray fluorescence was detected by a solid state Si(Li) detector. The photoacoustic signal was detected by a condenser microphone and was amplified by a lock-in amplifier.

Results and Discussion

Figure 4-3-2, A shows the simultaneously measured fluorescence and photoacoustic spectra for a 10μm thick copper sample. The spectra were normalized to the ion chamber current. Figure 4-3-2, B are intensity ratio plots. The E_o value obtained from extrapolation were 1.44 and 1.32 KeV for the K_α and K_β fluorescence respectively, resulting in a quantum yield of about 0.144 and 0.027 for

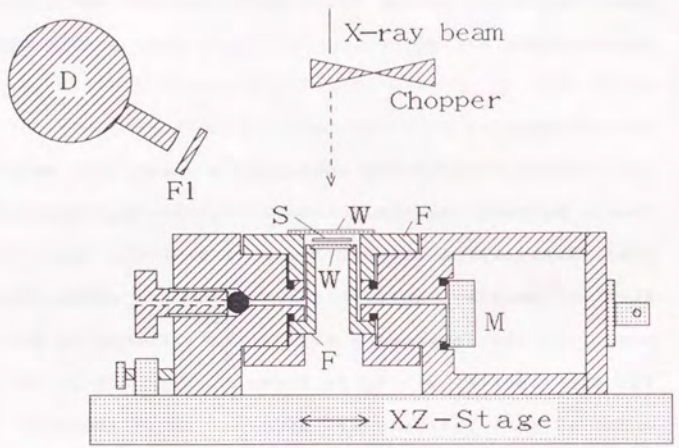

Fig. 4-3-1. A schematic diagram of the experimental setup and the photoacoustic cell for simultaneous measurements.
S, sample; W, Be windows; F, frame; M, microphone; Fl, Al filter; D, Si(Li) detector.

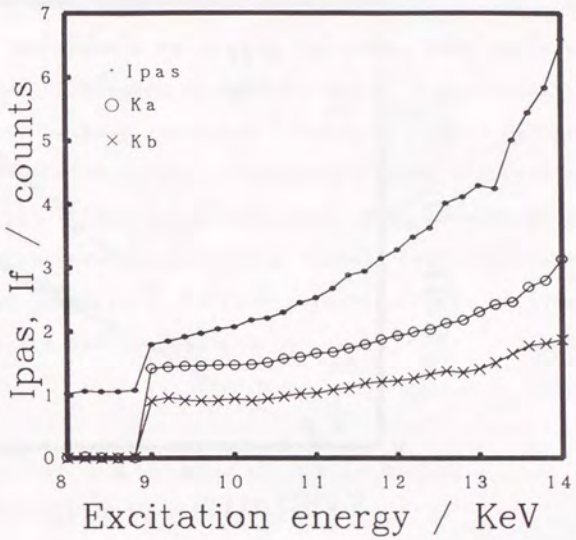

Fig. 4-3-2, A. Simultaneously measured photoacoustic and fluorescence excitation spectra for a 10μm thick copper sample.

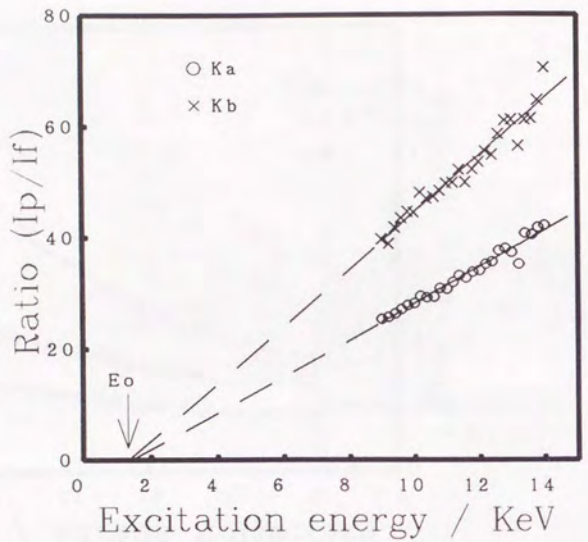

Fig. 4-3-2, B. Plots of the ratio of photoacoustic and fluorescent signal intensities as a function of excitation energy. Extrapolation is performed by least-square fitting.

the K_α and K_β fluorescence respectively. In this calculation, intensity ratio of the K_α and K_β fluorescence is assumed to be 5:1. The total quantum yield of K_α and K_β is about 0.17. This value is approximately half of the value reported (about 0.4) in the literatures[2, 3, 47, 48]. This is considered to be due to X-ray fluorescence self-absorption and also due to background noise in the photoacoustic spectra caused by L-absorption and/or window materials. Further investigation of these contributions are now in progress.

CHAPTER V

Application to Quantitative Analysis of Powdered Samples

Photoacoustic measurements are well known as a tool for spectral analysis of powdered samples without requiring any sample pretreatment. In the X-ray region, elemental analysis can be conducted since atoms have a characteristic absorption. One of the problems in quantitative measurements of powdered samples is that the photoacoustic intensity is influenced by the particle sizes of the powdered samples[63]. Three factors needed to be considered are stated as follows. One is the optical saturation, which is caused by complete absorption of the excitation beam by particles with the large absorbing power. The second is the thermal saturation, which is caused by heat generated in the deep region of the particle whose size is larger than the thermal penetration length. This type of heat does not contribute to the signal generation. The third is scattering of the excitation beam for fine particles, which reduces the absorption of light. The first and second factors can be avoided by using a high chopping frequency or pulverizing the sample into fine particles. The third factor is very serious in the visible light region. While the third factor is not serious in the X-ray region. Since the refractive index of materials for X-rays is nearly 1 so that the

scattering is small[2,64].

Measurements based on X-ray absorption are well suited for determination of heavy elements. In section 5-1, an attempt to determine the iron content in aluminum hydroxide gel by X-ray photoacoustic measurements at a fixed X-ray wavelength (1.504Å) will be presented with a discussion on the distribution of iron in a sample particle. This section is based on the published report.[65] In section 5-2, an approach to eliminating background will be discussed.

5-1 X-ray Photoacoustic Spectrometry Applied to Determination of Iron in Aluminum Hydroxide Gel

Introduction

In the X-ray region, elemental analysis can be conducted using the characteristic absorption of atoms. In particular, measurements based on X-ray absorption are well suited for the determination of heavy elements in a matrix which mainly consists of light elements[66]. Photoacoustic measurements are known to be suitable for spectral analyses of powdered samples. In this study an attempt was made to determine the iron in an aluminum hydroxide gel by photoacoustic measurements in the X-ray region. The mass absorption coefficient of iron for X-rays in the range of 8 to 20KeV is larger than that of the aluminum hydroxide matrix. Thus, X-ray absorption increases as the iron content increases. Moreover, the photoacoustic signal depends on the thermal diffusion length, μ, of the sample and the average depth of heat generation, d. The thermal diffusion length μ is a measure of a solid's ability to transfer heat to its surface and is expressed as

$$\mu = 2k / (2\pi f \rho C), \qquad (5.1.1)$$

where k, f, ρ and C are, the thermal conductivity of the sample, the chopping frequency, the density and the specific heat, respectively. In general, d corresponds to the optical

absorption length or the particle diameter of the sample The optical absorption length equals $1/\beta$, where β is the optical absorption coefficient of the sample. Theoretically,[7] the photoacoustic signal intensity varies as f^{-1} when $\mu > 1/\beta$ or $\mu > d$, and $f^{-3/2}$ when $\mu < 1/\beta$ and $\mu < d$. Therefore, the frequency response of the photoacoustic signal for a powder sample provides information concerning the diameter of powder particles or the distribution of iron in each powder particle.

Experimental

Photoacoustic measurements were conducted using synchrotron radiation (beam line BL-15A at the National Laboratory for High Energy Physics, KEK) as an excitation source. The X-ray beam was monochromated at 1.504Å and focused to about 2mm diameter on the sample. The photoacoustic cell used in this study is shown in Fig. 5-1-1. The powdered sample was packed in a concave shaped sample holder (18mm in diameter and about 0.5mm in depth) in the cell and covered with a poly-propylene based adhesive tape. The cell window and the bottom of the sample holder were made of thin Be plates (0.25mm and 0.5mm). The photoacoustic signal was detected by a condenser microphone attached to the cell where the signal was then sent to a lock-in amplifier (NF Circuit Block Inc. LI575). The photoacoustic

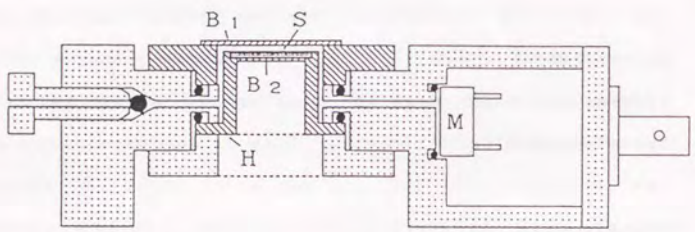

Fig. 5-1-1. Sectional view of the photoacoustic cell for measurement of the powder samples.
S:Sample, H:sample holder, B1:upper Be window, B2:lower Be window, M:microphone, ●:o-rings.

signal intensity was normalized to the X-ray beam intensity measured by an ion chamber positioned in front of the photoacoustic cell.

Ten grams of anhydrous aluminum chloride were dissolved in 400ml of deionized water; then the desired amount of iron(III) chloride solution and 20g of urea were added. The mixed solution was heated on a water bath for about one hour. Precipitated aluminum hydroxide gel was separated by filtration on a glass filter (G3 type) and washed with deionized water. The gel was dried for one day in an oven at 110℃ and ground to powder. The iron in the sample was determined by a UV-VIS spectrophotometric method with o-phenanthroline as a color reagent (λ_{max} =510nm). The water content in the sample was determined by thermogravimetric analysis (TGA) and differential thermal analysis (DTA). The analyses were carried out with a thermal analyzer (Shimadzu, DT-30) in the temperature range from room temperature to about 450℃ under the following conditions: a nitrogen atmosphere flow rate of 26.5cc/min, a heating rate of 15℃/min, weighted portions of 11.1 to 21.1mg, a TGA full scale ±25mg and a DTA full scale of ±25μV.

Results and Discussion

The results of the spectrophotometric and thermal

analyses are listed in Table 5-1-1. The iron content in the samples were found to be lower than the calculated values, since the gel contained a large amount of water. The results of DTA and TGA analysis are shown in Fig. 5-1-2. DTA analysis gave two broad endothermic peaks at about 70℃ and 250℃. These peaks were assigned to two types of water (adsorbed and dispersed water) in the gel. Aluminum hydroxide gel changes to active alumina ($Al_2O_3 \cdot nH_2O$: n=0-0.6) above 300℃[67]. In the calculation of the water content, it was assumed that the sample contained a certain amount of water above 450℃ and that n=0.6. The water content in the samples was determined by calculation of the weight loss in TGA analysis above 60℃, and is also shown in Table 5-1-1.

The photoacoustic signal intensities, I_P, are plotted in Fig. 5-1-3. as a function of the iron content, as determined by a spectrophotometric method in the visible light region. It was found that the background intensity was large at low chopping frequencies. The background intensity showed a tendency to decrease at high chopping frequencies. The photoacoustic signal of the aluminum hydroxide gel was estimated from the elemental composition of the sample. The mass absorption coefficients of Al, O, H and Fe at 1.504Å were found to be 44.9, 10.6, 0.43 and 288cm/g, respectively[1]. Under the conditions that the thickness of

Table 5-1-1. Iron and water contents in samples

Sample No	Fe*1	Fe*2	ρ	water content
	wt%	wt%	g/cm³	wt%
1	0	0.031	0.77	$10.8^{*3} + 58.6^{*4}$
2	1	0.537	0.70	$6.6^{*3} + 71.1^{*4}$
3	2	0.677	0.81	$5.2^{*3} + 70.5^{*4}$
4	3	0.939	0.66	$4.1^{*3} + 69.9^{*4}$

*1:calculated iron content, *2:determined iron content, ρ:density, *3:weight loss in the range from room temperature to 100℃, *4:weight loss above 120℃ up to 350℃.

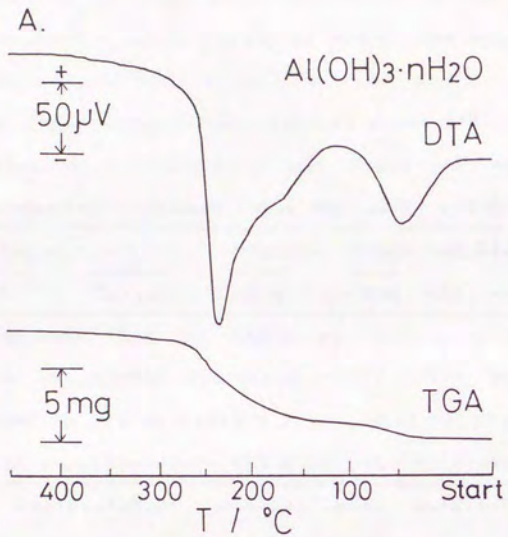

Fig. 5-1-2A. Results of thermogravimetric and differential thermal analysis for sample No-1 (sample without iron addition).

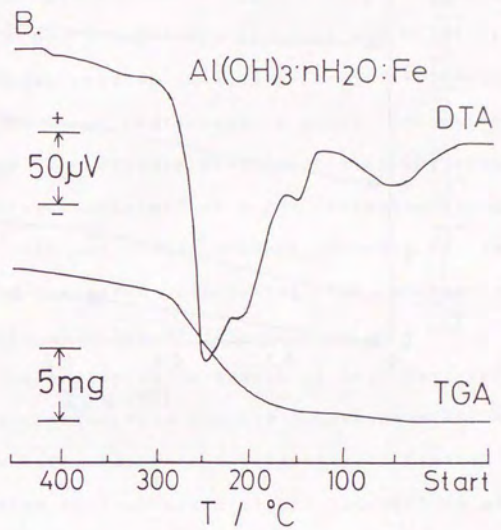

Fig. 5-1-2B. Results of thermogravimetric and differential thermal analysis for sample No-4 (sample with iron addition, Fe 0.939wt%).

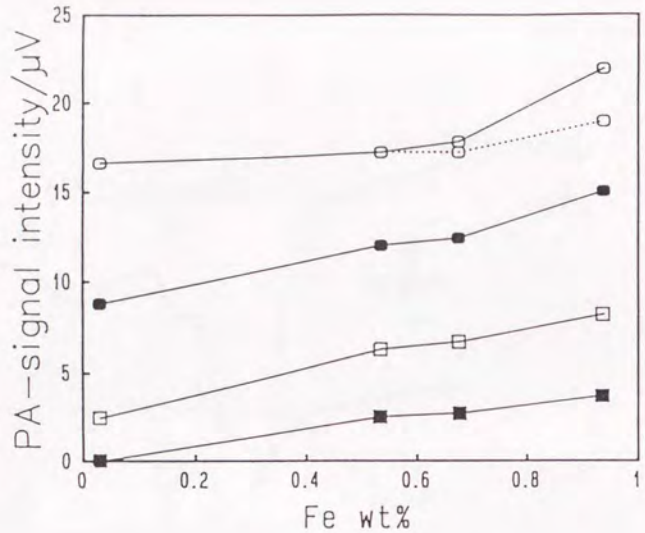

Fig. 5-1-3. Photoacoustic intensities *versus* iron content for various chopping frequencies. The estimated photoacoustic signal intensities are also plotted, which is normalized to the photoacoustic signal intensity of the sample without any addition of iron and at a chopping frequency of 10Hz.
—○—○— :10Hz, —●—●— :20Hz, —□—□— :40Hz,
—■—■— :80Hz, ···○···○·· :estimated value for 0.5mm sample thickness.

the sample was 0.5mm and that the thermal penetration depth was large compared to the particle size, the relative intensities of the photoacoustic signals were calculated as 1.000, 1.011, 1.051 and 1.113 for samples No 1 to 4, respectively. These results show that the contribution of iron atoms to the total photoacoustic signal intensity was considerably low. The results also roughly agree with the experimental results obtained at a low chopping frequency (1.000, 1.038, 1.075 and 1.338, f=10Hz). However, a further consideration is required concerning the excess sample intensity with the addition of iron.

The signal intensity for a sample without any addition of iron was subtracted from the raw photoacoustic signal intensities as the background intensity. Figure 5-1-4 shows the corrected photoacoustic signal intensities plotted as a function of iron content. It was found that plots for a high chopping frequency show good linearity and a low background contribution. This suggests that measurements at a high chopping frequency are preferable for quantitative analysis. If the iron was uniformly distributed in the sample, the relative photoacoustic signal at high chopping frequencies can be calculated by assuming the sample is thin. This is because the thermal diffusion length becomes short at high chopping frequencies. For example, the relative intensities for a sample of 0.1mm thickness were

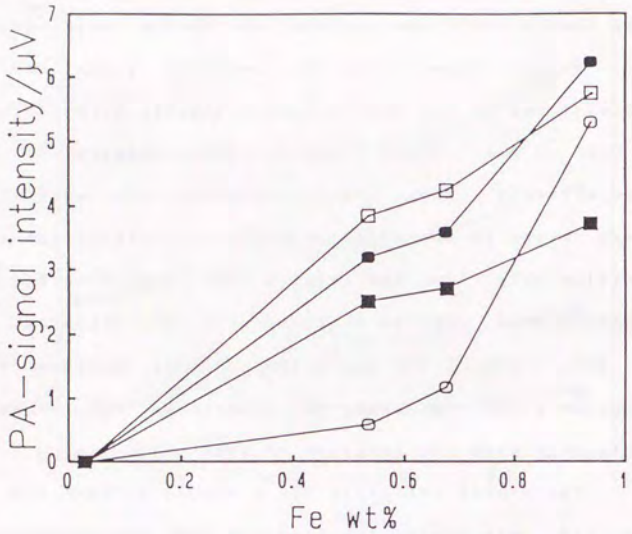

Fig. 5-1-4. Corrected photoacoustic intensities *versus* iron content for various chopping frequencies. Photoacoustic signal intensities estimated from the mass-absorption coefficient and the heat capacity are also plotted.
○:10Hz, ●:20Hz, □:40Hz, ■:80Hz.

calculated to be 1.000, 0.9996, 1.094 and 1.111. These values are not consistent with the experimental values, and suggest that the assumption of a uniform iron distribution in the sample is not valid.

Figure 5-1-5 shows the change in the signal intensity *versus* chopping frequency. The signal intensity decreases as f^{-1} for samples with iron additions (No-2, 3, 4). However, the signal intensity decreased as $f^{-3/2}$ for samples without iron (No-1). These two relationships between the photoacoustic signal intensity and the chopping frequency correspond to the two cases in RG theory[7]. One is the case where the sample is thermally thin and the other where the sample is thermally thick. Thus, the aluminum hydroxide gel powder without iron is thermally thick in this chopping frequency range, while the samples with iron added were thermally thin. This suggest that iron is concentrated at the surfaces of the particles. Microphotographs of the sample powder are shown in Fig. 5-1-6. A microphotographic observation showed that the prepared powder samples have a wide distribution over diameters ranging from few μm to about 100μm. It is also possible that the sample powder was not homogeneous and that the iron was concentrated in small particles. Thus, photoacoustic spectrometry in the X-ray region can give information concerning the elemental composition and distribution of elements in a powdered sample.

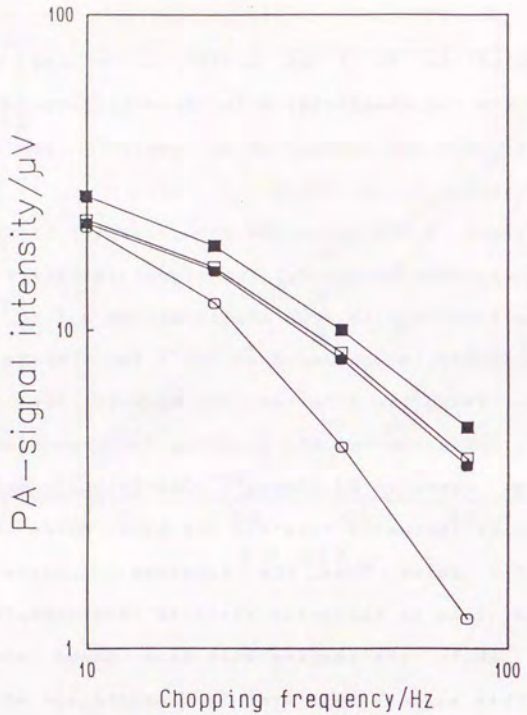

Fig. 5-1-5. Photoacoustic intensities *versus* chopping frequency.

○: sample No-1 (Fe 0.031wt%),

●: sample No-2 (Fe 0.537wt%),

□: sample No-3 (Fe 0.677wt%),

■: sample No-4 (Fe 0.939wt%).

A.

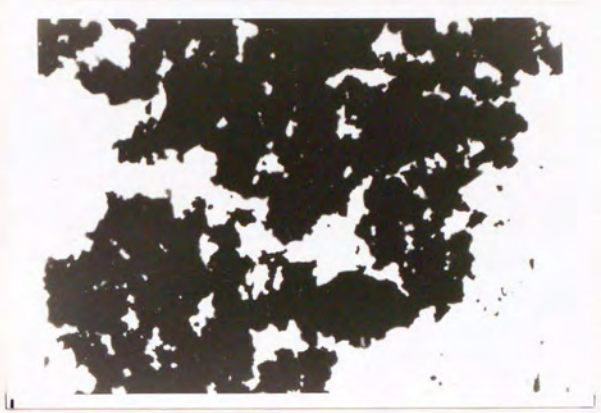

B.

Fig.5-1-6A,B. Microphotographs of powdered samples (×40).

A: sample No-1(Fe 0.031wt%),

B: sample No-2(Fe 0.537wt%).

C.

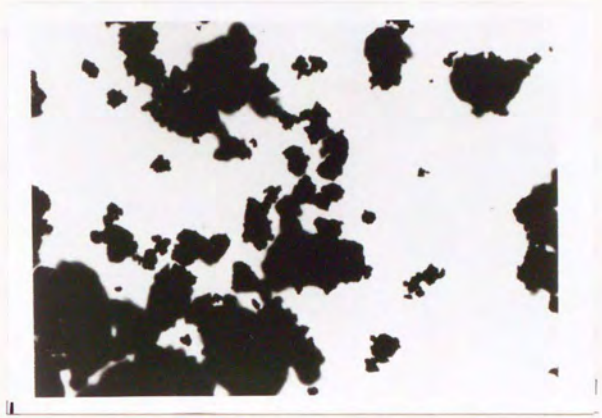

D.

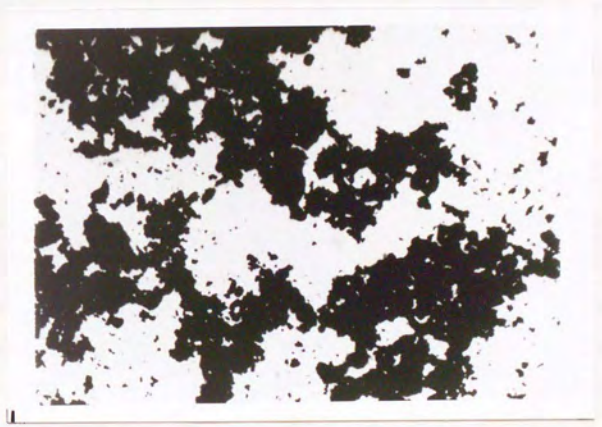

Fig.5-1-6C,D. Microphotographs of powdered samples (×40).
C:sample No-3(Fe 0.677wt%),
D:sample No-4(Fe 0.939wt%).

5-2 X-ray Photoacoustic Spectra of Powdered Samples

In section 5-1, it was demonstrated that the determination of iron in aluminum hydroxide gel can be made by X-ray photoacoustic measurement at a fixed X-ray wavelength (1.504Å). The background signal intensity, however, was not negligibly small. One of the approaches to eliminate the background contribution is to measure the absorption jump at the absorption edge of the target element[66]. In this section, we present examples of measuring the absorption jump of the Fe-K absorption edge in the X-ray photoacoustic spectra of powdered samples measured with a monochromatic X-ray beam.

Experimental

The photoacoustic measurements were conducted using synchrotron radiation (beam line BL-10C at National Laboratory for High Energy Physics, KEK) as an excitation source. The X-ray beam was monochromated at 1.70 to 1.80Å and focused to an area of about 3×8mm on the sample. The chopping frequency was 8Hz. Photoacoustic cell and detection system used in this study was the same as that shown in section 5-1 (Fig. 5-1-1). The powdered sample was packed in a concave shaped sample holder (18mm in diameter and about 0.5mm in depth) in the photoacoustic cell and covered with

poly-propylene based adhesive tape. The beam intensity was measured using copper foil (thickness 0.01mm) as an absorber, and the photoacoustic intensity of the sample powder was corrected for variations of the beam intensity.

The samples were iron sponge powder (Jhonson and Matthey) and active alumina powder. The active alumina powder was obtained from aluminum hydroxide gel powder containing a specified amount of iron by heating at about 600℃ under atmosphere. Iron in the active alumina powder was determined to be 0.02% and 1.72% by UV-VIS spectroscopy using o-phenanthroline as a color reagent (λ_{max} =510nm). The density of the active alumina powder and iron sponge powder were about 1.29 and 3.34 respectively. The particle size of the iron sponge was less than 100μm, while that of the active alumina ranged from about 10μm to 0.5mm.

Results and Discussion

Figure 5-2-1 shows the X-ray photoacoustic spectra obtained by sequentially changing the wavelength of the X-ray beam. The absorption edge of iron was observed for the iron sponge powder and the active alumina powder containing iron. The absorption edge can be designated with the magnitude and wavelength of the absorption jump. The wavelength of the measured absorption jump agreed with previously obtained values in the literature[1]. However, the

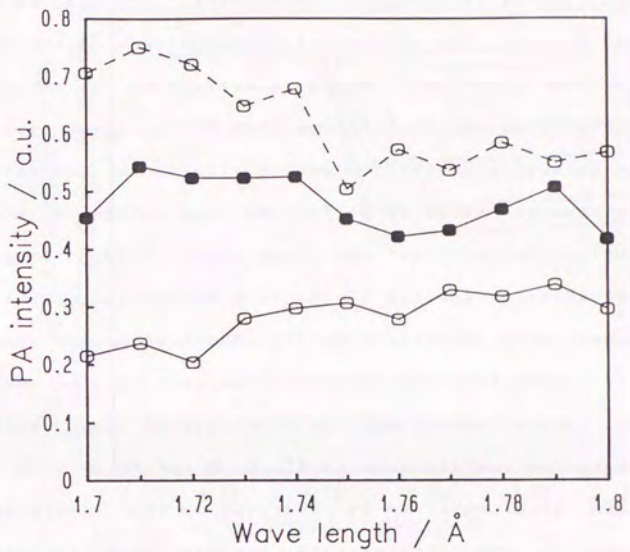

Fig. 5-2-1. X-ray photoacoustic spectra near the Fe K absorption edge.

—○—○— :active alumina (Fe 0.02wt%),

—●—●— :active alumina (Fe 1.72wt%),

---○---○--- :iron sponge.

magnitude of the jump was larger than the expected value. In this section, the measure of the magnitude of the absorption jump is given by R_J which is defined as the ratio of the intensity on the high energy side of the absorption edge to the intensity on the low energy side of the absorption edge. The observed value of R_J for the iron sponge and the active alumina with iron was 1.34 and 1.16, respectively. Photoacoustic spectra of the iron sponge and active alumina powder were calculated by the amount of X-rays absorbed in the sample from the elemental composition, the density of the sample powder and the thickness of the sample. Mass absorption coefficients of Al, O, H and Fe at 1.70, 1.75 and 1.80Å were obtained by referring to the literature[1] and those in the intermediate regions were estimated from interpolation and extrapolation. The relative intensity of the photoacoustic signal was calculated on the condition that the thermal penetration depth was large compared to the particle size. Figure 5-2-2 shows the expected photoacoustic spectra of iron sponge for various sample thickness. As shown in Fig. 5-2-2, absorption jumps are large for thin samples. R_J was calculated to be 1.78, 1.59, 1.36, 1.24, 1.04 and 1.00 for sample thicknesses of 0.05, 0.06, 0.08, 0.1, 0.2 and 0.5mm, respectively. According to the theory for photoacoustic signal generation[17], the effective sample thickness for signal generation is limited by the thermal

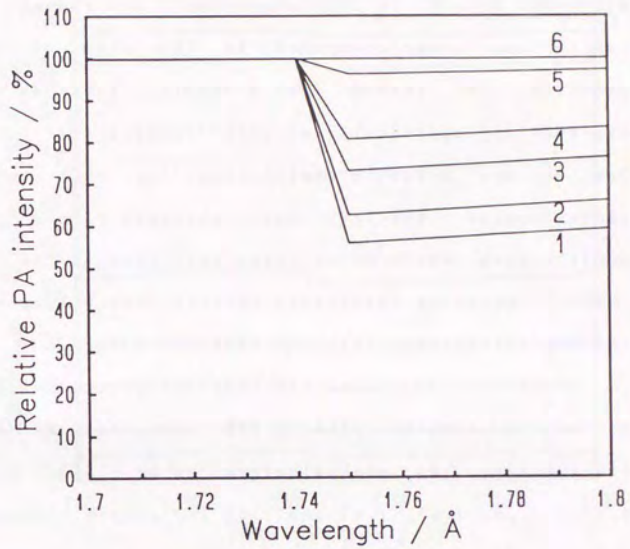

Fig. 5-2-2. Estimated X-ray photoacoustic spectra of iron sponge powder. Traces 1 to 6 correspond to spectra of sample thicknesses 0.05, 0.06, 0.08, 0.1, 0.2, and 0.5mm, respectively.

diffusion length. In this experiment, the thermal diffusion length was large compared to the size of the powder particle. The reason that a sample thickness of 0.08mm explains the empirically measured spectra well is not clear. One of the possible explanations is that the expected photoacoustic spectra was obtained from absorption coefficients which do not take into account the effect of EXAFS. Therefore the actual spectra show a larger rise at the absorption edge than the expected value.

Figure 5-2-3 shows the expected photoacoustic spectra of active alumina with 1.72% iron for various sample thicknesses. R_3 was calculated to be 1.13, 1.13, 1.12, 1.11, 1.10, 1.07, 1.03 and 1.02 for sample thicknesses of 0.01, 0.02, 0.04, 0.06, 0.1, 0.2 and 0.5mm, respectively. These results show that the measured R_3 was larger compared to the estimated R_3 for a 0.5mm thickness, and was the same as that estimated for a thickness of 0.01 and 0.02mm. It is considered that the effective sample thickness was smaller than the actual thickness. This is consistent with the results in section 5-1, where the photoacoustic intensities with addition of iron were larger than those estimated from the elemental composition, which was attributed to either concentration of iron clusters or surface segregation of iron. Another possible explanation may be attributed to the fine structure at the absorption edge.

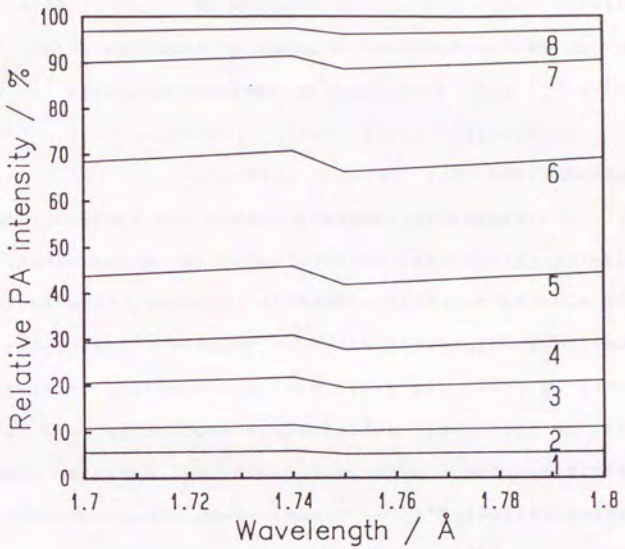

Fig. 5-2-3. Estimated X-ray photoacoustic spectra of active alumina powder with 1.72% iron. Traces 1 to 8 correspond to spectra for sample thicknesses of 0.01, 0.02, 0.04, 0.06, 0.1, 0.2, 0.4 and 0.6mm, respectively.

CHAPTER VI

X-ray Photoacoustic Imaging of Surface and Subsurface Structure of Layered Materials

Introduction

Photoacoustic signals depend on optical, thermal and elastic properties as well as on the geometrical shape of the sample. Photoacoustic imaging techniques for characterizing structured samples have been widely investigated[6]. In particular non-destructive observation of the surface and subsurface structure is of interest in characterizing materials such as ceramic coatings,[68] semiconductors,[69,70] subsurface grooves,[71] phase transitions[72] and subsurface defects of ceramics[73]. The photoacoustic image generally shows spatial variation in i) optical properties (coefficients of absorption, reflection and scattering), ii) thermal properties (thermal conductivity, heat capacity and thermal expansion factor) and iii) elastic properties of the sample[74]. The study of the thermal properties for a sample is well suited to photoacoustic spectroscopy. X-ray photoacoustic imaging is similar to those in the visible light region in the sense that the image reflects information on the thermal and elastic properties of a sample. X-rays penetrate deeply into materials and is insensitive to sample surface because

the refractive index of materials is nearly 1 for X-rays. Therefore, X-ray excitation seems to be more suitable for the imaging of subsurface structures than visible excitation[75]. Furthermore, since X-ray absorption is characteristic of the chemical element and the optical properties in the X-ray region differ from those in the visible region, it is of interest to measure the photoacoustic images in both of these wavelength regions.

This chapter is based on a previously published report[76].

Experimental

Experiments in the X-ray region were conducted using synchrotron radiation at beam line BL-15A of the Photon Factory (Tsukuba, Ibaraki, Japan). The beam was monochromated at 1.504Å. Figure 6-1 shows a schematic diagram of the experimental setup. The X-ray beam was narrowed with the use of a 1mm lead pinhole and was chopped with a rotating sector. The photoacoustic cell used in this experiment was the same as that described in chapter 4-1. The cell windows and the cell body were made of beryllium and brass, respectively. The photoacoustic cell was mounted. The photoacoustic signal was detected by a condenser microphone and then amplified by a lock-in amplifier (NF CIRCUIT BLOCK INC., LI575). The amplitude and

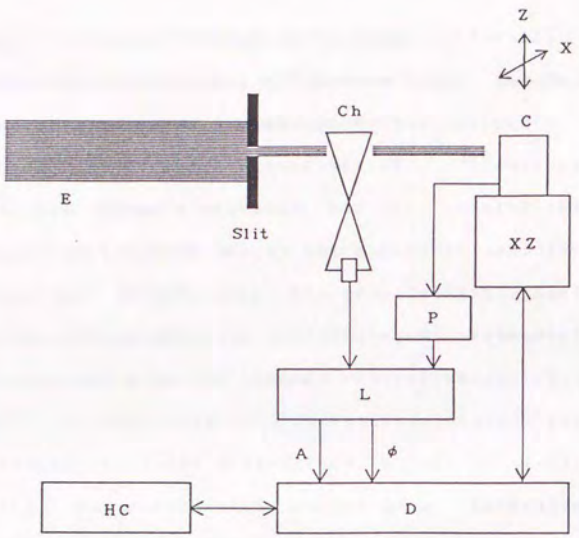

Fig. 6-1. Schematic diagram of the experimental set up for X-ray photoacoustic imaging.
E, monochromatic X-ray beam of synchrotron radiation; Ch, chopper; C, photoacoustic cell; XZ, computer controlled XZ-stage; P, preamplifier; L, lock-in amplifier; D, desk top computer with A/D converter; HC, hardcopy.

phase output signals of the lock-in amplifier were led to an analog-to-digital converter and stored in a computer memory (NEC, PC9801). Data acquisition times ranging from 30 to 60 seconds were required to obtain a desirable photoacoustic image since the X-ray beam was narrowed by the lead pinhole resulting in an intensity loss. The XZ-scanning of the sample position was controlled by the computer. Each step of the scanning was set to 1mm or 0.5mm. In the former case, the imaging area was divided into 16×16 points and in the latter case the imaging area was divided into 32×32 points. In the case of photoacoustic measurements with visible or UV light excitation, the upper beryllium window of the cell was replaced with a 1mm thick quartz window. The light beam from a 500W xenon arc lamp was filtered with an UV cut (TOSHIBA, Y44) or UV pass (TOSHIBA, UVD36B) filter and focused to a spot of about 1mm in diameter on the specimen. IR components in the beam was removed with the use of an IR cut (TOSHIBA, IRA-25S) filter.

Samples.

A laminated sheet of aluminum and lead foil and a flexible print circuit board were used as samples. In the case of the laminated sample, pieces of aluminum foil (thickness about 15μm, diameter 18mm) were made to adhere on the two sides of a piece of lead foil (thickness 100μm,

a.

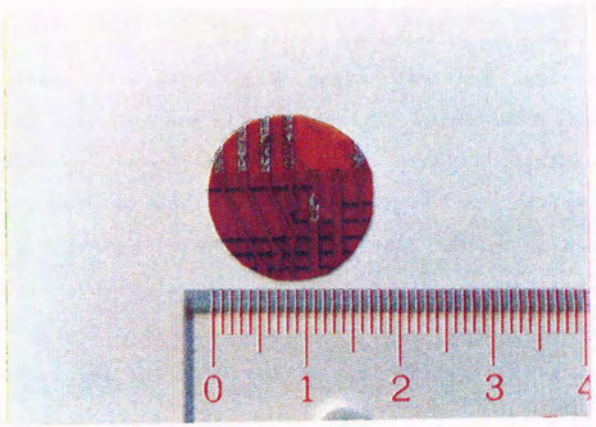

b.

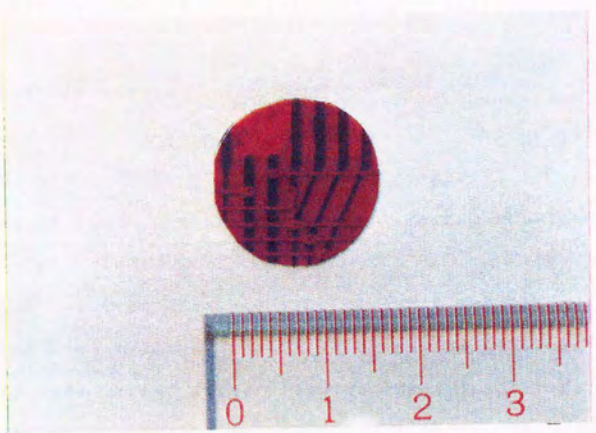

Fig. 6-2. Photographs of a flexible printed circuit board.
a, X-ray exposed face and b, back side.

diameter 18mm) by cyanoacrilate resin. The lead layer had a rectangular hole (3×4mm) at the center. Figure 6-2 shows a photographs of the flexible print circuit board. The flexible print circuit board consisted of basically 3 layers: i) orange colored polymer base, ii) copper print circuit strip or colorless polymer layers on both sides of the base, and iii) orange colored surface polymer layers on both sides of the print circuit board. The thickness of each layer was about 50μm. The bare part of the print pattern of copper strip was coated with soft metallic solder.

Results and Discussion

Figure 6-3 shows X-ray photoacoustic images of the laminated sample made of aluminum and lead foil. For each data point, a data acquisition time of 30s was required. The imaging area (15×15mm^2) was divided into 16×16 points (256pixels) and the XZ-stage step size was set to be 1mm. The hole at the center of lead foil below the surface layer is clearly seen in the figure. In the signal amplitude image (Fig. 6-3a), the signal intensity is weak in the central part of the specimen and strong in the surrounding area. On the contrary, as shown in Fig. 6-4a, signal intensity for the visible light excitation is strong at the central part and weak in the surrounding area. These results are interpreted as follows. i) X-ray absorption mainly

a.

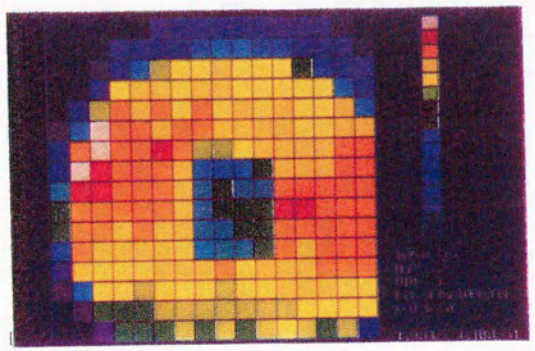

b.

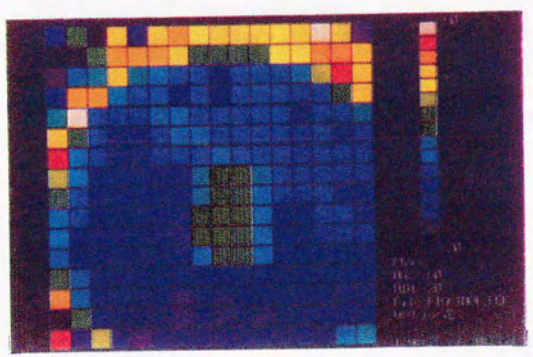

Fig. 6-3. X-ray photoacoustic images of the lead / aluminum laminated sample.
a, amplitude image and b, phase image.

a.

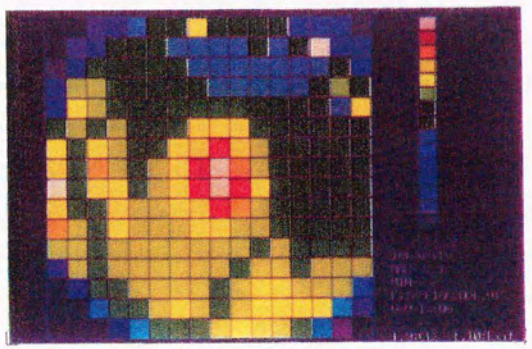

b.

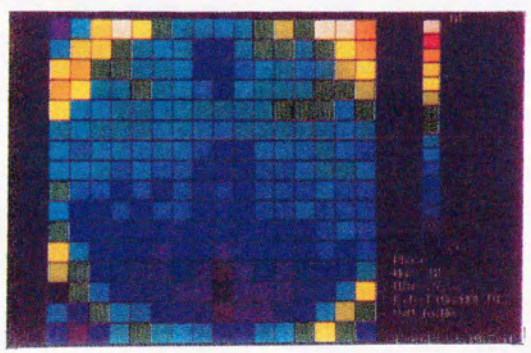

Fig. 6-4. Visible light photoacoustic images of the lead / aluminum laminated sample.
a, amplitude image and b, phase image.

occurred in the lead foil and consequently the signal is weak in the central part where the lead foil is missing. ii) The absorption of the visible light occurred only at the aluminum foil surface, so that the heat generated uniformly over the whole surface of the specimen. The thermal properties, however, are not uniform over the whole surface due to the presence of the lead foil beneath, and that the heat loss due to heat diffusion into the lead foil occurs only in the peripheral part of the sample. Consequently, the photoacoustic signal is intense in the central part of the sample.

In the X-ray photoacoustic image of the phase signal (Fig 6-3b), the phase delay is small in the central part of the specimen and large in the surrounding area. On the contrary, as shown in Fig. 6-4b, the visible light excitation phase delay is large in the central part of the specimen and small in the surrounding area. These results are also interpreted as follows. i) In the surrounding part of the specimen, X-ray absorption mainly occurs in the lead foil which is at deeper level of the specimen and consequently the phase delay is large. In the central part of the specimen, X-ray absorption occurs only in the surface aluminum layer and the phase delay is small. ii) Absorption of visible light occurs over the whole surface of the aluminum foil. In the surrounding area, however, the heat

loss occurs due to heat diffusion in the lead foil, resulting in the immediate decrease of the surface temperature, so that the heat delay is larger in the central part and smaller in the peripheral, cool part of the specimen.

The results obtained in the experiments above show that the mechanism of the photoacoustic signal with X-ray excitation is somewhat different from that with visible light excitation. In the imaging experiments with X-ray excitation, the obtained images reflect the variation of the amount of heat generated in the specimen, while the images with visible light excitation reflect the variation of the rate of heat diffusion in the specimen.

Figure 6-5 shows X-ray photoacoustic images of a flexible printed-circuit board. The chopping frequency was 29Hz. Data acquisition time was 60s for each data point. The imaging area ($15.5 \times 15.5 mm^2$) was divided into 32×32 points (1024pixels) and the XZ-stage step size was 0.5mm. The printed copper stripes coated with solder were observed in the images of the signal amplitude and phase delay. The print-circuits in the lower part of the specimen are covered with a polymer coating, which is also seen in the intensity and phase images. In the image of the phase delay, the printed-circuits on the surface show a small phase delay. On the other hand, the printed circuits at the subsurface layer

a.

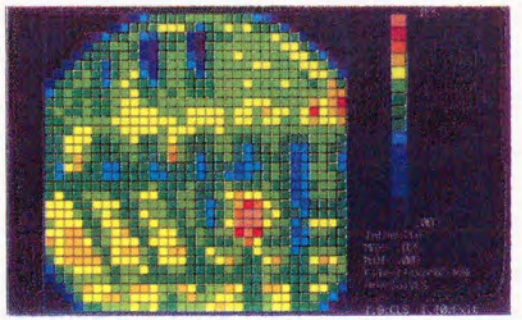

b.

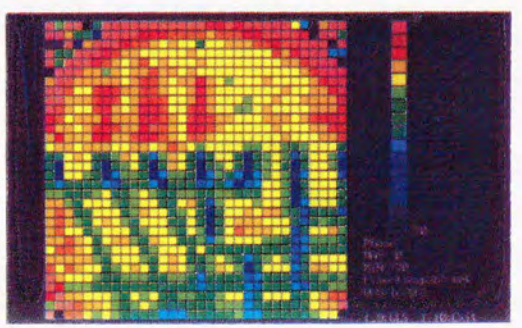

Fig. 6-5. X-ray photoacoustic images of the flexible printed circuit board.
a, amplitude image and b, phase image.

were observed to have patterns corresponding to a large phase delay.

On the other hand, in the photoacoustic images with UV light excitation, as shown in Fig. 6-6, the signal intensity is weaker in the copper print pattern than the other part of the specimen. In the signal phase images (Fig. 6-6b), the print pattern below the polymer layer was seen more clearly than in the amplitude image. These results are considered to be due to the high reflectance of the soft metallic coating on the print pattern and large heat diffusivity of the subsurface copper patterns.

a.

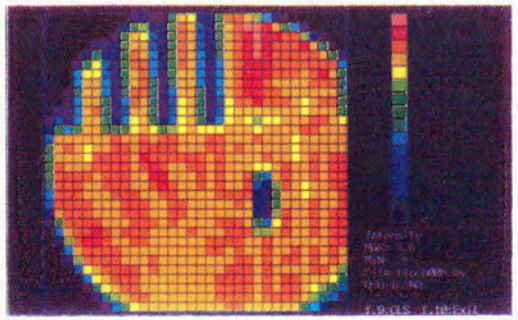

b.

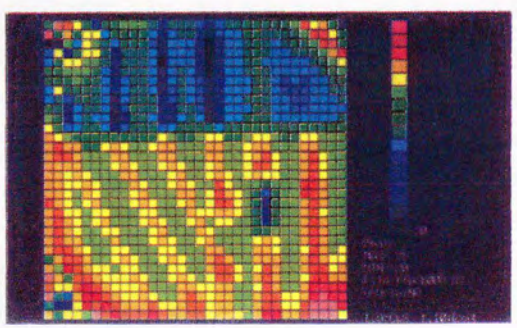

Fig. 6-6. Photoacoustic images of the flexible printed circuit board with UV light excitation.
a, amplitude image and b, phase image.

Summary and Future Trends

Photoacoustic experiments in the X-ray wavelength region were successfully conducted with the use of both synchrotron radiation (SR) and a conventional X-ray tube as excitation sources. Photoacoustic measurements using the monochromated X-rays of synchrotron radiation is excellent as an element-specific technique that compliments the conventional photoacoustic technique in the UV-IR region. While, photoacoustic measurements with the use of a conventional X-ray tube, however, are also important in its convenience of operation and accessibility. In the photoacoustic measurements, thermal and elastic properties of samples are often of interest as in the chapters III or VI where layered structure samples were studied. It is noticeable that the refractive index for materials in the X-ray region is approximately unity. Therefore, in the X-ray region one may observe the inner part of the sample without problem inherent in the surface reflection and diffusion.

In particular, photoacoustic method can measure true absorption of X-rays in the materials and can give informations about total flow of absorbed energy. Various X-ray induced phenomena such as fluorescence, photo-reactions, phase transitions, dislocation and photocurrent will be the object of the photoacoustic technique. Furthermore, since

photoacoustics is not a detector limited branch of spectroscopy, it will surely be extended into the soft X-ray region. New excitation sources such as synchrotron radiation using undulator are very intense in the soft X-ray region.

In this thesis, experiments involving the X-ray photoacoustic effect in the fields of analytical chemistry and materials science were presented. In these fields, only the surface has been scratched indicating some of the possible applications of this technique to these diverse disciplines. In the near future, it is quite possible that photoacoustics will become a common and useful analytical and research technique for many scientists engaged in the use of X-rays as a spectroscopic tool and as a nonspectroscopic probe of thermal and elastic properties. Its ease of operation and versatility can only increase its areas of applications. Examples of some new areas are:

(1) soft X-ray studies of biological, organic and inorganic compounds (modification of a PAS cell for the soft X-ray region should be quite straightforward, but photothermal deflection method or photothermal radiation method are promising in the sense that no cells and no windows are needed in these method,);

(2) depth profiling and imaging using an X-ray tube, of opaque materials such as metals and composite materials of metal and organic-polymers that cannot be readily examined

by conventional optical techniques;

(3) the field of catalysis, where the characterization of heterogeneous metal oxides and oxide mixtures of powdered form may prove to be an important application;

(4) the field of biology where the PAS technique can be used to study the effect of X-ray dosage in-situ for biological systems both in the laboratory and in the field, providing data that can now only be obtained after extensive estimation of X-ray absorbance and concentration of components in the sample.

In the X-ray region, new sources such as laser plasma X-ray and synchrotron radiation using undulator or wiggler have been developed and will be soon available for the excitation source. Furthermore, X-ray lasers are now in the process of development. Photon flux of these new sources will be 10^3 times or more intense than that of the conventional synchrotron radiation, and use of these new sources will solve the problems of X-ray photoacoustics which arise from insufficiency of X-ray flux. Focusing technique of X-rays and transform techniques such as Hadamard transform technique will improve the signal-to-noise ratio and spatial resolution in X-ray photoacoustic imaging, and will make it convenient and, moreover, precise.

The next few years should be an exciting period of growth for photoacoustic spectroscopy in the X-ray region.

References

1) C. H. Macgillary, G. D. Rieck and K. Lonsdale, "*International Tables for X-ray Crystallography*, Vol. 3", p. 175, Kynoch Press, Birmingham, England, 1962.

2) A. H. Compton and S. K. Allison, "*X-rays in Theory and Experiment*", p477, D. Van Nostrand, USA 1936.

3) W. Bambynek, B. Crasemann, R. W. Fink, H. U. Freund, H. Mark, C. D. Swift, R. E. Price and P V. Rao, *Rev. Modern Phys.*, 44, 717 (1972).

4) A. E. Hughes and D. Pooley, "*Real Solid and Radiation*", p100, The Wykeham Publications, London, 1975.

5) A. C. Tam, *Review of Modern Phys.*, 58, 381 (1986).

6) A. Rosencwaig, "*Photoacoustics and Photoacoustic Spectroscopy*", John Wiley & Sons, New York, 1980.

7) A. Rosencwaig and A. Gersho, *J. Appl. Phys.*, 47, 64 (1976).

8) M. J. Adams and G. F. Kirkbright, *Analyst*, 102, 678 (1978).

9) K. Kato, Y. Kobayashi, S. Aoki, Y. Sugitani, *Anal. Sci.*, 3, 275 (1987).

10) K. Kato, T. Takei and Y. Sugitani, *Anal. Sci.*, 6, 481 (1990).

11) D. Duston, R. W. Clark, J. Davis and J. P. Apruzese, *Phys. Rev.*, 27, 1441 (1983).

12) D. L. Matthews et. al., *Phys. Rev. Lett.*, 54, 110 (1985).

13) M. H. Key, *Nature*, 316, 314 (1985).

14) S. Suckewer et. al., *Phys. Rev. Lett.*, 55, 1753 (1985).

15) *Photon Factory Actibity Report 1986*, #5, p90, National Laboratory for High Energy Physics (1987).

16) *Photon Factory Activity Report 1988*, #7", pR-14, pR-25, National Laboratory for High Energy Physics (1989).

17) A. Rosencwaig, "*Optoacoustic Spectroscopy and Detection*" Chap. 8, ed. by Y. H. Pao, Academic Press, New York (1977).

18) R. Germer, *Rev. Sci. Instrum.*, 55, 1463 (1984).

19) T. Masujima et al., *Chem. Lett.*, 1987, 973 (1987).

20) "*Kagakubinran kisohen* II" 2nd ed, ed. by Chem. Soc. of Japan, Maruzen, Tokyo (1975).

21) A. C. Boccara, D. Fournier and J. Badoz, *Appl. Phys. Lett.*, 36, 130 (1980).

22) J. C. Murphy and L. C. Aamodt, *J. Appl. Phys.*, 51, 4580 (1980).

23) K. Kato, S. Ishino and Y. Sugitani, *Chem. Lett.*, 1980, 783 (1980).

24) Y. Sugitani, A. Uejima and K. Kato, *J. of Photoacoust.*, 1, 217 (1982).

25) K. Kato and Y. Sugitani, *Anal. Sci.*, 4, 59 (1988).

26) K. Kato and Y. Sugitani, *Anal. Sci.*, 6, 177 (1990).

27) M. B. Robin, "*Optoacoustic Spectroscopy and Detection*", Chap. 7, ed. by Y. H. Pao, Academic Press, New York (1977).

28) M. J. Adams and G. F. Kirkbright, *Spectroscopy Lett.*, 9, 255 (1976).

29) M. H. Butterfield, G. F. Bryant and J. Dowsing, *Trans. Soc. Instr. Tech.*, 13, 111 (1967).

30) "*Correlation Function and Spectra* (in japanese)", ed. by T. Isobe, Tokyo Univ. Press, (1967).

31) H. P. Hsu, "*Fourier Analysis*", Simon & Schuster, New York (1970).

32) J. Kondo, "*Fourier Transform and its Application* (in japanese)", Baifukan, Tokyo (1974).

33) G. F. Kirkbright, R. M. Miller and Y. Sugitani, *Anal. Chem.*, 56, 2043 (1984).

34) A. Uejima and Y. Sugitani, *J. Photoacoustic.*, 1, 397 (1983).

35) H. S. Carslaw and J. C. Jaeger, "*Conduction of Heat in Solids*", 2nd edition, Oxford (1953).

36) "*RIKAGAKU JITEN*" 4th edition, Iwanami Shoten, Tokyo Japan (1987).

37) Y. Sugitani, S. Aoki, K. Kato and Y. Kobayashi, "*Springer Series in Opt. Sci.* 58, *Photoacoustic and Photothermal Phenomena*", p31, Springer Verlag, (1987).

38) K. Kato and Y. Sugitani, *Anal. Sciences*, 5, 545 (1989).

39) K. Tohji, Y. Udagawa M. Harada and A. Ueno, *Nippon Kagaku Kaishi*, 1986, 1553 (1986).

40) N. R. Lokhande and C. Mande, *J. Phys. Chem. Solid*, 43, 731 (1982).

41) T. Masujima, et. al. *Photon Factory Activity Report 1986*, 6, 139 (1987).

42) K. Kato and Y. Sugitani, *Bull. Chem. Soc. Jpn.*, 52, 3733 (1979).

43) K. Kato and Y. Sugitani, *Bull. Chem. Soc. Jpn.*, 52, 3499 (1979).

44) K. Kato and Y. Sugitani, *Photon Factory Activity Report 1989*, 8, 56 (1990).

45) K. Ohno, A. Kawase and T. Nakamura, "*Ekkususen Bunsekihou* (in Japanese)", p. 22, Kyoritsu-shuppan, Tokyo, (1987).

46) J. N. Demas and G. A. Crosby, *J. Phys. Chem.*, 75, 991 (1971).

47) W. Hanke, J. Wernisch and C. Pohn, *X-ray Spectrometry*, 14, 43 (1985).

48) J. Byrne and N. Howarth, *J. Phys. B*, 3, 280 (1970).

49) M. J. Adams, J. G. Highfield and G. F. Kirkbright, *Anal. Chem.*, 49, 1850 (1977).

50) M. Morita, *Jpn. J. Appl. Phys.*, 20, 295 (1981).

51) J. C. Murphy and L. C. Aamodt, *J. Appl. Phys.*, 48, 3502 (1977).

52) R. S. Quimby and W. M. Yen, *J. Appl. Phys.*, 51, 1780 (1980).

53) W. Lahmann and H. J. Ludewig, *Chem. Phys. Lett.*, 45, 177 (1977).

54) K. Kato and Y. Sugitani., *Chem. Biomed. Environ. Instrumentation*, 11, 85 (1981).

55) J. G. Fairchild, *Am. Mineral.*, 141, 265 (1929).

56) Y. Sugitani, H. Kasuya, K. Nagashima and S. Fujiwara, *Nippon Kagaku Zasshi*, 90, 52 (1969).

57) For instance, H. Strunz, "*Mineralogische Tabellen*", Akad. Verlag., Leipzig (1957).

58) Y. Sugitani, K. Kato and K. Nagashima, *Bull. Chem. Soc. Jpn.*, 52, 918 (1979).

59) J. T. Bell and R. E. Biggers, *J. Mol. Spectrosc.*, 25, 312 (1968).

60) E. Rabinowitch and R. L. Belford, "*Spectroscopy and Photochemistry of Uranyl Compounds*", Macmillan, New York (1964).

61) S. P. McGlynn and J. K. Smith, *J. Mol. Spectrosc.*, 6, 164 (1961).

62) H. D. Burrows and T. J. Kemp, *Chem. Soc. Rev.*, 1974, 139.

63) E. M. Monahan Jr. and A. W. Nolle, *J. Appl. Phys.*, 48, 3519 (1977).

64) S. Aoki, "*Ekkususenbunseki no Shinpo* XVI", p209, Ed. by Jpn. Soc. Anal. Chem., (1984).

65) K. Kato and Y. Sugitani, *Anal. Sci.*, 5, 697 (1989).

66) H. A. Liebhafsky, H. G. Pfeiffer, E. H. Winslow and P. D. Zemany, "*X-ray Absorption and Emission in Analytical Chemistry*" Chapter 3, John Wilew & Sons, New York, (1960).

67) "*Shin Jikken Kagaku Koza*, Vol. 8", p. 247, Chem. Soc. of Japan, Maruzen, Tokyo, (1976).

68) M. Liezers and R. M. Miller, "*Springer Series in Optical Sciences Vol. 58, Photoacoustic and Photothermal Phenomena*", p437, Springer Verlag, (1987).

69) N. Mikoshiba, H. Nakamura and K. Tsubouchi, *Oyo Butsuri*, 58, 483 (1985).

70) K. Kubota and H. Murai, *J. Appl. Phys.*, 56, 835 (1984).

71) M. Izuchi, H. Nakano and S. Nagai, *Jpn. J. Appl. Phys.*, 26, 221 (1987).

72) S. Kojima, *Jpn. J. Appl. Phys.*, 24, 1571 (1985).

73) I. Tomeno and H. Ohzu, *Jpn. J. Appl. Phys.*, 24, 1445 (1985).

74) A. Rosencwaig, *J. Appl. Phys.*, 51, 2210 (1980).

75) R. W. Ryon, et al., *Adv. X-ray Anal.*, 31, 35 (1988).

76) K. Kato and Y. Sugitani, *Anal. Sci.*, 7, 296 (1991).

Acknowledgments

The author gratefully dedicates this thesis to the late Professor Kozo Nagashima, who introduced the author to the field of analytical chemistry when he was the author's academic adviser at the Tokyo University of Education.

The author also wishes to express his hearty thanks to Professor Yoshinori Sugitani of Kanagawa University for his invaluable advice, helpful guidance and critical comments not only on this work but also on previous studies concerning this work.